Object kinetic Monte Carlo modelling of irradiation microstructures with elastic interactions

Thomas Jourdan

Object kinetic Monte Carlo modelling of irradiation microstructures with elastic interactions

T. Jourdan

Université Paris-Saclay, CEA, Service de Recherches de Métallurgie Physique, 91191, Gif-sur-Yvette, France

E-mail: thomas.jourdan@cea.fr

Abstract.

Elastic interactions between point defects and sinks, such as dislocations and cavities, affect the diffusion of point defects and are responsible for some of the features observed in microstructures under irradiation. It is therefore necessary to include elastic interactions in kinetic simulations for a quantitative prediction of material properties. In this work a method is presented to accurately and efficiently evaluate the strain field in object kinetic Monte Carlo simulations. It can handle any strain field which is biharmonic, such as the one generated by a dislocation segment or a cavity in isotropic elasticity. A speed-up of several orders of magnitude is obtained compared to the direct summation over strain sources, so that simulations over experimental time scales can be performed within reasonable computation times. The case of a thin foil containing a high density of loops under irradiation is investigated. Loop growth rates are found to depend on the loop radius, as shown experimentally, but more complex effects due to the surrounding microstructure are also highlighted.

Introduction

Microstructure evolution under irradiation is known to be driven by the large supersaturation of vacancies and self-interstitial atoms (SIAs) [1]. These point defects migrate to pre-existing sinks, such as dislocations, grain boundaries and surfaces, or agglomerate with each other, which typically leads to the formation of cavities and dislocation loops. The sustained growth of both vacancy and SIA clusters when only Frenkel pairs are generated by irradiation has been successfully explained by the dislocation bias model [2]. This model relies on the fact that SIAs interact more strongly with elastic fields due to their larger distortion field, and therefore diffuse preferentially towards dislocations and dislocation loops, which create long-range elastic fields compared to cavities. Modelling precisely the diffusion of point defects to the various sinks of the microstructure is therefore important to predict quantitatively the growth rate of dislocation loops and cavities, from which void swelling rates can be deduced [3].

Object kinetic Monte Carlo (OKMC) has been successfully used to model the growth kinetics of vacancy and SIA clusters [4, 5, 6, 7, 8]. However, in most cases elastic fields were not taken into account. They were included in OKMC only in a few studies, considering that sinks do not evolve [9, 10, 11, 12, 13, 14], more rarely with full account of sink evolution [15, 16]. To model the preferential absorption of SIAs by dislocations without including the elastic field, a larger absorption region around dislocations is generally adopted regarding SIAs. Beyond this absorption region, point defects perform a pure random walk, *i.e.* the diffusion is not biased by elastic fields. This approach is very efficient, since all jump frequencies are the same whatever the point defect location in the matrix, but it relies on a parameter, the extent of the absorption region, which must be determined by dedicated elastic bias calculations [10, 13]. Elastic biases depend on the temperature, sink size in the case of dislocation loops and cavities, so in general a tedious parametrization task is necessary to cover all relevant cases. In addition biases are assumed not to depend on the surrounding microstructure, which has proven to be erroneous [17, 16]. Taking into account explicitly the elastic interactions in OKMC appears necessary to obtain results in quantitative agreement with experimental results.

Performing efficient OKMC simulations with elastic interactions is not an easy task. OKMC relies on the fast evaluation of jump frequencies, which becomes problematic when they depend on the interaction of point defects with the local elastic field. Within linear elasticity, it is convenient to obtain this local field by summing individual contributions of all point defects and sinks in the system. This approach becomes more and more expensive as the number of sinks in the system increases, or if periodic boundary conditions (PBCs) are used. Indeed, due to the long range of the fields generated by dislocations, it is not possible to use a cutoff distance for their evaluation. In practice, it is nearly impossible to reach realistic simulation times if the field changes after each defect jump.

Calculations may become considerably more tractable if the strain field of point defects and point defect clusters which are mobile can be neglected. This is usually the case if these mobile objects remain small. For example, in fcc metals Frank loops are immobile and their strain field, within the dipolar approximation, is proportional to the number of SIAs which form them. For typical sizes of several nanometers, it is orders of magnitude larger than the strain field of SIAs or small mobile SIA clusters. Therefore, if the concentration of mobile species is not too high, their contribution to the field can be safely ignored. This assumption will be made in the rest of this work. Since the field is unchanged after the jump of a defect, it may be advantageous to use techniques which evaluate the field on a grid‡. The local field, after each defect jump, can be calculated efficiently by interpolation of the values at the grid points. The field is updated only when the sink microstructure changes, due to the absorption or emission of a mobile species. The calculation of the field on the grid may be costly, so this approach is especially useful when jump events are much more frequent than absorption and emission events by sinks. This is true except at very low temperature (high sink density) and high temperature (high emission rate of defects by sinks).

Calculating the field on a grid can be done efficiently by two main techniques. The first one is to solve the problem in Fourier space, using fast Fourier transform (FFT) [18]. It has been done successfully in phase field [19, 20] and discrete dislocation dynamics simulations (DDD) [21, 22]. However this method requires some care to avoid numerical artifacts due to the FFT grid [23]. Since the elastic field can vary quite sharply, in particular close to sinks, a dense grid is required to obtain reliable point defect trajectories in OKMC. This can become unnecessarily expensive for large systems with low sink density.

The other technique is the fast multipole method (FMM) [24]. Although it is often used as an order N method to calculate the field at the location of the sources, it gives a local expansion of the field on a grid, which can be used in the present case to evaluate the local field at the position of mobile species. An upper bound for the error on the field can be defined rigorously and an adaptive version of the algorithm [25] permits to reduce the memory footprint and computation time when sources are heterogeneously distributed. Several flavours of the FMM have been used in DDD [26, 27, 28].

In this article a method based on the FMM is presented to calculate efficiently the elastic field in OKMC simulations. It enables the simulation of large elastically isotropic systems with common sinks observed in irradiated microstructures (cavities, dislocations, dislocation loops, stacking fault tetrahedra, etc.). We show that this real space approach is particularly convenient to simulate systems with heterogeneous distributions of sinks, or with free surfaces. As an application we simulate the evolution of dislocation loops in aluminum. We show that interstitial loops do not necessarily all

‡ One could even envisage to precalculate the field on all atomic sites. Due to memory constraints, this can only be done on small systems. This method is especially useful when the microstructure does not evolve with time [12]. Otherwise an update of the field on each lattice site is necessary after a change in the microstructure, which may become computationally expensive.

grow under irradiation, in contradiction with previous OKMC and rate theory models, but in agreement with experiments.

1. OKMC modelling with elastic interactions

1.1. Jump frequencies of point defects in presence of an elastic field

OKMC is a method which is well adapted to simulate the evolution of microstructures under irradiation. It relies on a database of known events, which are of several types: creation of new defects by irradiation, jump of a point defect from a stable position to another one, thermal emission of a point defect. Events are performed sequentially following the standard residence time algorithm [29, 30]. Elastic interactions between point defects and sinks alter the frequency of events. For example, the jump frequency of a point defect from $\boldsymbol{x} = (x_1, x_2, x_3)$ to $\boldsymbol{x} + \boldsymbol{h}$ can be written as

$$\nu^{\boldsymbol{h}}(\boldsymbol{x}) = \nu_0 \exp\left(-\frac{\Delta E^{\boldsymbol{h}}(\boldsymbol{x})}{k_{\mathrm{B}}T}\right), \tag{1}$$

where ν_0 is an attempt frequency and $\Delta E^{\boldsymbol{h}}$ is the activation energy, which reads

$$\Delta E^{\boldsymbol{h}}(\boldsymbol{x}) = E^{\mathrm{m}} + E^{\mathrm{int,s}}(\boldsymbol{x} + \boldsymbol{h}/2) - E^{\mathrm{int,e}}(\boldsymbol{x}). \tag{2}$$

In this expression, E^{m} is the migration energy without elastic interactions, $E^{\mathrm{int,e}}$ and $E^{\mathrm{int,s}}$ are the interaction energies for stable and saddle configurations, respectively. Here the saddle position is assumed to be located halfway between the two stable positions. A similar dependency of emission rates on elastic interactions exists [31] and will not be detailed here.

To lowest order, the interaction energy of a point defect with a strain field ε_{ij} depends on the elastic dipole of the point defect P_{ij} [32, 33] (summation on repeated indexes is implied):

$$E^{\mathrm{int}}(\boldsymbol{x}) = -P_{ij}\varepsilon_{ij}(\boldsymbol{x}). \tag{3}$$

For anisotropic defects, the elastic dipole depends on the defect orientation. It is in general different for stable and saddle configurations.

Within linear elasticity, the strain field can be calculated at any point by summing the strain contributions of all objects in the microstructure.

1.2. Strain sources

As discussed previously, the interaction between point defects or small mobile point defect clusters is not considered in this work. This is in general justified by the fact that the strain field due to large objects is much more intense. There is no difficulty to add this contribution of point defects as dipole-dipole interactions. However, in general the efficiency of the code would be considerably reduced due to the update of the field after any event affecting a point defect. Expressions of strain fields created by three

common objects, a dislocation loop, a dislocation segment and a cavity, are recalled in this section, in the framework of isotropic elasticity. The shear modulus and Poisson's ratio are noted μ and ν, respectively. Only the solution in an infinite medium is given; surface effects are treated in Section 3.2.

1.2.1. Dislocation segment and dislocation loop We follow the approach by Ghoniem and Sun [34] to give explicit expressions for the strain. To derive the strain field, we start from Mura's formula, which expresses the derivative of the displacement field $\boldsymbol{u}$ created by a dislocation loop [35, 36] as a line integral over the perimeter of the loop $\mathcal{C}$ (see also Fig. 1):

$$\frac{\partial u_i}{\partial x_j} = u_{i,j} = \epsilon_{jnh} b_m C_{pqmn} \oint_{\mathcal{C}} \frac{\partial}{\partial x_q} G^{\infty}_{ip}(\boldsymbol{x} - \boldsymbol{x'}) \, \mathrm{d}x'_h, \tag{4}$$

where ϵ_{ijk} is the permutation tensor, $\boldsymbol{b}$ is the Burgers vector, G^{∞}_{ij} is the elastic Green function in an infinite body, and C_{ijkl} are the elastic constants.

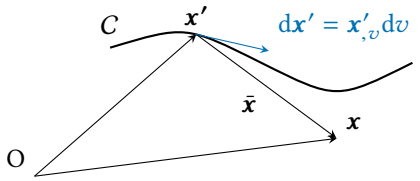

Figure 1. Notations used for a curved dislocation $\mathcal{C}$.

For an isotropic material, the elastic Green function is given by ($\bar{\boldsymbol{x}} = \boldsymbol{x} - \boldsymbol{x}'$, $\bar{x} = |\bar{\boldsymbol{x}}|$):

$$G^{\infty}_{ij}(\bar{\boldsymbol{x}}) = \frac{1}{16\pi(1-\nu)\mu} \left(\delta_{ij} \frac{3-4\nu}{\bar{x}} + \frac{\bar{x}_i \bar{x}_j}{\bar{x}^3} \right) = \frac{1}{4\pi\mu} \frac{\delta_{ij}}{\bar{x}} - \frac{1}{16\pi\mu(1-\nu)} \frac{\partial^2}{\partial x_i \partial x_j} \bar{x}. \tag{5}$$

In this equation δ_{ij} is the Kronecker delta.

Elastic constants can be written as

$$C_{pqmn} = \mu \left(\delta_{pm}\delta_{qn} + \delta_{pn}\delta_{qm} \right) + \frac{2\nu\mu}{1-2\nu} \delta_{pq}\delta_{mn}, \tag{6}$$

and since $\varepsilon_{ij} = 1/2 \left(u_{i,j} + u_{j,i} \right)$ the strain reads [34]:

$$\varepsilon_{ij}(\bar{\boldsymbol{x}}) = \frac{1}{8\pi} \oint_{\mathcal{C}} \left[-\frac{1}{2} (\epsilon_{jkl} b_i \bar{x}_{,l} + \epsilon_{ikl} b_j \bar{x}_{,l} - \epsilon_{ikl} b_l \bar{x}_{,j} - \epsilon_{jkl} b_l \bar{x}_{,i})_{,pp} + \frac{\epsilon_{kmn} b_n \bar{x}_{,mij}}{1-\nu} \right] \mathrm{d}x'_k. \tag{7}$$

The parametric form of $\boldsymbol{x}'(v)$ given by Ghoniem and Sun is used:

$$\boldsymbol{x}'(v) = \boldsymbol{q}_i \mathcal{N}_i(v), \tag{8}$$

where $\mathcal{N}_i(v)$ are basis functions, v is a parameter and $\boldsymbol{q}_i$ are generalized coordinates. The differential reads

$$\mathrm{d}x'_k = x'_{k,v} \mathrm{d}v = q_{ik} \mathcal{N}_{i,v}(v) \mathrm{d}v. \tag{9}$$

Using quadrature to evaluate the integral, the strain can be numerically computed by summing over a finite number of strain sources:

$$\varepsilon_{ij}(\bar{\boldsymbol{x}}) \approx \frac{1}{8\pi}\sum_{\alpha=1}^{N_\mathrm{q}} w_\alpha \left[-\frac{1}{2}(\epsilon_{jkl}b_i\bar{x}_{,l} + \epsilon_{ikl}b_j\bar{x}_{,l} - \epsilon_{ikl}b_l\bar{x}_{,j} - \epsilon_{jkl}b_l\bar{x}_{,i})_{,pp}(v_\alpha) + \frac{\epsilon_{kmn}b_n\bar{x}_{,mij}(v_\alpha)}{1-\nu}\right] x'_{k,v}(v_\alpha), \tag{10}$$

where N_q is the number of quadrature points and w_α are the quadrature weights. In the following Gauss-Legendre quadrature is used.

This expression can be simplified, since some terms are zero and $\bar{x}_{,ijk}$ is invariant by permutation. The expressions can be given, for example, as a function of $\bar{x}_{,111}$, $\bar{x}_{,112}$, $\bar{x}_{,113}$, $\bar{x}_{,123}$, $\bar{x}_{,221}$, $\bar{x}_{,222}$, $\bar{x}_{,223}$, $\bar{x}_{,331}$, $\bar{x}_{,332}$ and $\bar{x}_{,333}$ (similar simplications were performed for the stress in [34]). Explicit expressions of the strain components are given in Appendix A.

For a circular dislocation loop of radius r, located at the origin, and whose normal to its habit plane is $\boldsymbol{n}$, the following coordinates can be chosen:

$$\boldsymbol{q}_1 = r\begin{pmatrix} \frac{n_2^2}{1+n_3} + n_3 \\ -\frac{n_1 n_2}{1+n_3} \\ -n_1 \end{pmatrix} \qquad \boldsymbol{q}_2 = r\begin{pmatrix} \frac{-n_1 n_2}{1+n_3} \\ \frac{n_1^2}{1+n_3} + n_3 \\ -n_2 \end{pmatrix} \tag{11}$$

and the basis functions are ($v \in [-1,1]$ for Gauss-Legendre quadrature)

$$\mathcal{N}_1(v) = \cos(\pi v) \qquad \mathcal{N}_2(v) = \sin(\pi v). \tag{12}$$

Expression (10) can also be used for a dislocation segment. In this case,

$$\boldsymbol{q}_1 = \boldsymbol{x}_1 \qquad \boldsymbol{q}_2 = \boldsymbol{x}_2, \tag{13}$$

where $\boldsymbol{x}_1$ and $\boldsymbol{x}_2$ are the end points of the segment and the basis functions are ($v \in [-1,1]$)

$$\mathcal{N}_1(v) = \frac{1}{2}(1-v) \qquad \mathcal{N}_2(v) = \frac{1}{2}(1+v). \tag{14}$$

1.2.2. Cavity Let us consider a cavity of radius r, which contains some gas with pressure p, located at $\boldsymbol{x}'$. The strain field created by this cavity in the matrix, at $\boldsymbol{x}$ ($\bar{x} > r$), is [37, 38]

$$\varepsilon_{ij}(\bar{\boldsymbol{x}}) = \left(p - \frac{2\hat{\gamma}}{r}\right)\frac{1}{4\mu}\left(\frac{r}{\bar{x}}\right)^3\left[\delta_{ij} - 3\frac{\bar{x}_i\bar{x}_j}{\bar{x}^2}\right], \tag{15}$$

where $\hat{\gamma}$ is the surface tension of the metal.

It can also be written under the following form, which is more convenient for use in the FMM:

$$\varepsilon_{ij}(\bar{\boldsymbol{x}}) = -\left(p - \frac{2\hat{\gamma}}{r}\right)\frac{1}{4\mu}r^3\frac{\partial^2}{\partial x'_i\partial x'_j}\left(\frac{1}{\bar{x}}\right). \tag{16}$$

Contrary to the dislocation segment and the dislocation loop, the strain is calculated exactly by using a single strain source located at $\boldsymbol{x}'$.

2. Fast calculation of the strain field

2.1. Calculation of the field using local expansions and FMM

Following Eq. (16), any component of the strain field generated by a cavity can be written as a derivative of $1/\bar{x}$, so it is harmonic. A general solution to $\Delta\phi = 0$ is

$$\phi(\boldsymbol{x}) = \sum_{l=0}^{\infty} \sum_{m=-l}^{l} \left(L_{lm} x^l Y_l^m(\theta,\varphi) + M_{lm} \frac{Y_l^m(\theta,\varphi)}{x^{l+1}} \right) \tag{17}$$

$$= \sum_{l=0}^{\infty} \sum_{m=-l}^{l} \left(L_{lm} R_l^m(x,\theta,\varphi) + M_{lm} I_l^m(x,\theta,\varphi) \right), \tag{18}$$

where Y_l^m are the spherical harmonics (see Appendix B, Eq. (B.1)), R_l^m and I_l^m are the regular and irregular solid harmonics, respectively. If the strain field is evaluated at $\boldsymbol{x}$ with $x < x'$, multipole expansion coefficients M_{lm} are all zero and only local expansion coefficients L_{lm} are useful. In this case Eq. (18) is called a local expansion. It can be truncated to a given value of l to give an approximate value of the strain field.

The strain field generated by a dislocation segment depends on the derivatives of $\bar{x}$ (Eq. (7)), so it is not harmonic in general. However, $\bar{x}$ is a solution to the biharmonic equation. This is also the case of its derivatives. Any solution ψ to the biharmonic equation can be written as [39]

$$\psi(\boldsymbol{x}) = \phi(\boldsymbol{x}) + x^2 \omega(\boldsymbol{x}), \tag{19}$$

where ϕ and ω are harmonic functions. So for a microstructure containing dislocations and cavities, if all strain sources are such that $x' > x$, any strain field component can be evaluated by a local expansion of the following type:

$$\psi(\boldsymbol{x}) = \sum_{l=0}^{\infty} \sum_{m=-l}^{l} L_{lm}^{(0)} R_l^m(x,\theta,\varphi) + x^2 \sum_{l=0}^{\infty} \sum_{m=-l}^{l} L_{lm}^{(2)} R_l^m(x,\theta,\varphi). \tag{20}$$

Compared to a Taylor expansion of the field, this decomposition is more compact: if the summation is performed up to order p, the number of terms is $O(p^2)$, whereas a cartesian expansion requires $O(p^3)$ terms. Since a fast evaluation of the local expansion is crucial in the KMC algorithm, using spherical harmonics is particularly interesting.

The FMM offers a rigorous framework to evaluate a field using local expansions with a prescribed accuracy. It is based on a hierarchical set of boxes forming a mesh, which can be uniform or adaptive. In the adaptive version, boxes are sub-divided in child boxes until the number of sources in each box is lower than a threshold $n_{\max}$. The case of a uniform mesh is shown schematically in Fig. 2. The field at $\boldsymbol{x}$, inside box b, is obtained by summing two terms. The first one is a local expansion as in Eq. (20), which contains the contribution of all sources located in boxes "well separated" from b (in blue). In particular, it contains information on periodic images of the simulation box and more generally on boundary conditions (see section 3). The second term is a direct sum over

the other sources (in orange), using expressions (10) and (15). Using local expansions only for boxes which are well separated from b ensures that local expansions converge. Cubic boxes are considered well separated if they do not share a boundary point. In this case, the minimal distance between the centers of boxes is $d_{\min} = 2/\sqrt{3}(r_b + r_b)$, where r_b is the radius of the smallest sphere enclosing b. This worst case can be used to define well-separated boxes when they are not cubic, by imposing that they are distant from each other by at least $d_{\min}$. It is the criterion used in our FMM implementation, which handles non-cubic boxes.

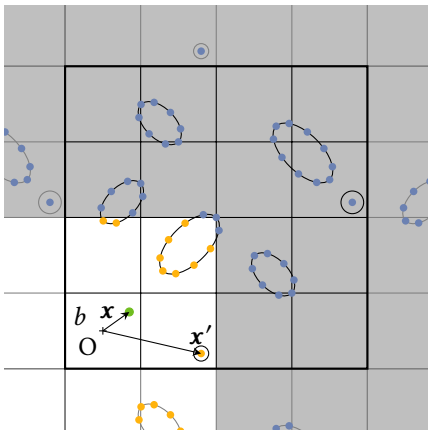

Figure 2. Schematic view of the calculation of the strain field using FMM in a microstructure containing dislocation loops and cavities. The contribution of blue sources, located in boxes which are well-separated from box b, containing the target point, is accounted for in a local expansion whose origin is the center of b. The contribution of other sources (in orange) is calculated with expressions (10) and (15).

The core of the FMM is the fast determination of local expansions. It relies on operations on multipole expansions of the fields. Once they are calculated for childless boxes, multipole expansions are translated and merged at lower levels of the hierarchy (upward pass) and converted into local expansions. Local expansions are then translated until they are expressed with respect to the center of childless boxes (downward pass). Details can be found, for example, in Ref. [25].

The FMM for harmonic fields, based on expansions in spherical harmonics, has been amply discussed [24, 40]. In particular, it has been optimised to speed up the conversion of multipole expansions into local expansions, using rotation of expansions and exponential representations [25]. For biharmonic fields, Gumerov and Duraiswami have proposed a modified version of the FMM, based on the decomposition in harmonic fields given in Eq. (19) [39]. This algorithm uses the classical operations on harmonic fields and includes an additional step due to the x^2 factor in Eq. (19). Since the definition of spherical harmonics in the present work differs from the one they used, translation and conversion formulas are given in Appendix C. The version implemented in this work includes rotation of expansions [41].

The FMM requires the calculation of multipole expansions of the field created by

a set of sources. In addition, for the adaptive version, which is used here, calculation of local expansions directly from sources is also necessary. Coefficients of the expansions are given for cavities and dislocation segments in the following sections.

2.2. Multipole expansion for a cavity

To obtain the multipole expansion of the strain field generated by a cavity, it is convenient to use the following expansion of the coulombic potential [42]:

$$\frac{1}{\bar{x}} = \sum_{l=0}^{\infty} \sum_{m=-l}^{l} x'^{l} Y_l^{-m}(\theta', \varphi') \frac{Y_l^m(\theta, \varphi)}{x^{l+1}} = \sum_{l=0}^{\infty} \sum_{m=-l}^{l} R_l^{-m}(x', \theta', \varphi') I_l^m(x, \theta, \varphi). \tag{21}$$

Inserting this expression in Eq. (16) yields the following multipole expansion for the strain field of a cavity:

$$\varepsilon_{ij}(\boldsymbol{x}) = \sum_{l=0}^{\infty} \sum_{m=-l}^{l} M_{lm} I_l^m(x, \theta, \varphi), \tag{22}$$

with

$$M_{lm} = -\left(p - \frac{2\hat{\gamma}}{r}\right) \frac{1}{4\mu} r^3 \frac{\partial^2}{\partial x_i' \partial x_j'} R_l^{-m}(x', \theta', \varphi'). \tag{23}$$

Second derivatives of regular solid harmonics are given in Appendix E.

2.3. Local expansion for a cavity

Coefficients of the local expansion are obtained straightforwardly from the previous section: the strain field reads

$$\varepsilon_{ij}(\boldsymbol{x}) = \sum_{l=0}^{\infty} \sum_{m=-l}^{l} L_{lm} R_l^m(x, \theta, \varphi), \tag{24}$$

with

$$L_{lm} = -\left(p - \frac{2\hat{\gamma}}{r}\right) \frac{1}{4\mu} r^3 \frac{\partial^2}{\partial x_i' \partial x_j'} I_l^{-m}(x', \theta', \varphi'). \tag{25}$$

Second derivatives of irregular solid harmonics are given in Appendix D.

2.4. Multipole expansion for a dislocation segment

As can be seen from Eq. (10), the multipole expansion of the strain field of a dislocation segment is readily deduced from the expansion of $\bar{x}_{,ijk}$. Since $\bar{x}$ is a solution to the biharmonic equation, it can be expressed as in Eq. (19) [39]. With our convention for spherical harmonics, we have, for $x > x'$:

$$\bar{x} = \sum_{l=0}^{\infty} \sum_{m=-l}^{l} \frac{1}{2l+3} x'^2 R_l^{-m}(x', \theta', \varphi') I_l^m(x, \theta, \varphi) + x^2 \sum_{l=0}^{\infty} \sum_{m=-l}^{l} \frac{-1}{2l-1} R_l^{-m}(x', \theta', \varphi') I_l^m(x, \theta, \varphi). \tag{26}$$

The derivatives $\bar{x}_{,ijk} = -\bar{x}_{,i'j'k'}$ can thus be written under the following form:

$$\bar{x}_{,ijk} = \sum_{l=0}^{\infty} \sum_{m=-l}^{l} M_{lm}^{(0)} I_l^m(x,\theta,\varphi) + x^2 \sum_{l=0}^{\infty} \sum_{m=-l}^{l} M_{lm}^{(2)} I_l^m(x,\theta,\varphi), \tag{27}$$

with

$$M_{lm}^{(0)} = -\frac{1}{2l+3} \frac{\partial^3}{\partial x'_i \partial x'_j \partial x'_k} \left(x'^2 R_l^{-m}(x',\theta',\varphi') \right) \tag{28}$$

$$M_{lm}^{(2)} = \frac{1}{2l-1} \frac{\partial^3}{\partial x'_i \partial x'_j \partial x'_k} \left(R_l^{-m}(x',\theta',\varphi') \right). \tag{29}$$

Derivatives of regular solid harmonics in Appendix E may be used to obtain more convenient expressions of multipole expansion coefficients.

2.5. Local expansion for a dislocation segment

As for multipole expansions, local expansions can be calculated from the following expression of $\bar{x}$ (for $x < x'$):

$$\bar{x} = \sum_{l=0}^{\infty} \sum_{m=-l}^{l} \frac{-x'^2}{2l-1} I_l^{-m}(x',\theta',\varphi') R_l^m(x,\theta,\varphi) + x^2 \sum_{l=0}^{\infty} \sum_{m=-l}^{l} \frac{1}{2l+3} I_l^{-m}(x',\theta',\varphi') R_l^m(x,\theta,\varphi). \tag{30}$$

The local expansion of $\bar{x}_{,ijk} = -\bar{x}_{,i'j'k'}$ is

$$\bar{x}_{,ijk} = \sum_{l=0}^{\infty} \sum_{m=-l}^{l} L_{lm}^{(0)} R_l^m(x,\theta,\varphi) + x^2 \sum_{l=0}^{\infty} \sum_{m=-l}^{l} L_{lm}^{(2)} R_l^m(x,\theta,\varphi), \tag{31}$$

with

$$L_{lm}^{(0)} = \frac{1}{2l-1} \frac{\partial^3}{\partial x'_i \partial x'_j \partial x'_k} \left(x'^2 I_l^{-m}(x',\theta',\varphi') \right) \tag{32}$$

$$L_{lm}^{(2)} = -\frac{1}{2l+3} \frac{\partial^3}{\partial x'_i \partial x'_j \partial x'_k} \left(I_l^{-m}(x',\theta',\varphi') \right). \tag{33}$$

Derivatives of irregular solid harmonics in Appendix D may be used to obtain more convenient expressions of local expansion coefficients.

2.6. Comparison with other FMM approaches for isotropic elasticity

The FMM has already been used to calculate elastic fields generated by dislocation ensembles. The first implementation for three dimensional DDD used expansions in cartesian coordinates [26]. As previously discussed, this approach is not optimal here

since local expansions are evaluated with $O(p^3)$ operations. On the contrary, the evaluation of an expansion in regular solid harmonics requires only $O(p^2)$ operations.

The FMM based on spherical harmonics, which was initially developed for the harmonic potential $1/\bar{x}$, has been used for other interaction potentials. Fu *et al.* [43] showed that harmonic FMM can be used for interaction potentials of the form

$$\mathcal{F}(\mathcal{Q}(\boldsymbol{x}')/\bar{x}, \boldsymbol{x}), \tag{34}$$

where $\mathcal{Q}$ is a function depending on data related to sources only and $\mathcal{F}$ is a linear operator on $\mathcal{Q}(\boldsymbol{x}')/\bar{x}$. In general several harmonic FMM calls must be combined to generate the field. In practice, some identities are useful to write potentials depending on derivatives of $\bar{x}$, such as the elastic Green function and its derivatives, under the form given by Eq. (34) [43, 44]. For example, the third derivatives can be written as [27]:

$$\bar{x}_{,ijk} = \left(x_k \frac{\partial^2}{\partial x_i \partial x_j} + \delta_{jk}\frac{\partial}{\partial x_i} + \delta_{ki}\frac{\partial}{\partial x_j}\right)\left(\frac{1}{\bar{x}}\right) - \frac{\partial^2}{\partial x_i \partial x_j}\left(\frac{x'_k}{\bar{x}}\right). \tag{35}$$

From Eq. (10), the strain field generated by a single source on a dislocation segment can be expressed as

$$\varepsilon_{ij}(\bar{\boldsymbol{x}}) = q^{ij}_{rst}\bar{x}_{,rst}. \tag{36}$$

Inserting Eq. (35) into Eq. (36), we obtain:

$$\varepsilon_{ij}(\bar{\boldsymbol{x}}) = \left(x_t \frac{\partial^2}{\partial x_r \partial x_s} + \delta_{st}\frac{\partial}{\partial x_r} + \delta_{rt}\frac{\partial}{\partial x_s}\right)\left(\frac{q^{ij}_{rst}}{\bar{x}}\right) - \frac{\partial^2}{\partial x_s \partial x_t}\left(\frac{q^{ij}_{rst}x'_t}{\bar{x}}\right). \tag{37}$$

It can be seen that without any optimisation, the calculation of one component of the strain field requires 36 harmonic FMM calls (27 for $q^{ij}_{rst}/\bar{x}$ and 9 for $q^{ij}_{rst}x'_t/\bar{x}$). This is significantly more expensive than the approach adopted here, which requires only 2 harmonic calls per component. Recently, Chen *et al.* [28] used the same decomposition of $\bar{x}$ as Fu *et al.* [43] to develop an FMM for the calculation of the stress field induced by dislocation segments. However no details concerning the implementation were provided.

The number of FMM calls is limited in our approach because the derivatives are taken with respect to the source variables x'_i instead of the target variables x_i (see Eqs. (22)-(23) and (27)-(29)). A similar technique was already used for the calculation of the magnetic field generated by magnetic dipoles [45]. Another advantage of this method is that any harmonic or biharmonic field can be included in the present formalism without requiring additional FMMs. If the derivatives are taken on the target variables and if the fields are not derived the same way, one must keep track of the nature of the sources, thereby increasing the number of FMMs.

3. Periodic boundary conditions and free surfaces

In OKMC simulations, PBCs may be used for self-defect migration, in order to simulate the microstructure evolution in the bulk of large systems, where the effect of free surfaces

or grain boundaries can be locally neglected. Accordingly, the contribution of the elastic fields from the sources in the image boxes must be summed to provide the field due to a periodic layout of strain sources. We describe in section 3.1 how to perform this summation efficiently with FMM and to ensure that it converges to a correct value.

Considering some boundaries of the simulation box as free surfaces is another interesting case. This situation is representative of thin foils observed in transmission electron microscopy, which are a few hundred nanometers thick. The above expressions of the strain field induced by cavities and dislocation segments correspond to isolated defects in an infinite medium. A correction to the elastic field calculated by FMM is necessary to ensure that it corresponds to a system with free surfaces (section 3.2).

3.1. Periodic boundary conditions: removing the spurious dipolar contribution

To sum the contributions of periodic images, we extend the upward pass of the FMM to lower "macroscopic" levels of hierarchy and obtain the multipole expansions of larger and larger clusters of the initial simulation box [46]. The downward pass is performed from macroscopic levels down to the highest levels of hierarchy, with interaction lists containing boxes located in image simulation boxes. This simple method permits to add the elastic field of a large number of periodic image boxes at low computation cost.

However, it is known that the field obtained by direct summation over image boxes is not necessarily absolutely convergent. In some cases the value of the sum depends on the way the summation is performed and may not correspond to a periodic solution [47]. For example, let us consider the strain fields created by dislocation loops and cavities, which decay as $1/\bar{x}^3$ for large values of $\bar{x}$. The summation is only conditionally convergent if it is performed along the three directions of space. Cai *et al.* have shown that the strain field corresponding to a periodic solution $\varepsilon_{ij}^{\mathrm{PBC}}$ differs from the field obtained by direct summation by a constant field $\boldsymbol{\varepsilon}^0$ [47]:

$$\varepsilon_{ij}(\boldsymbol{x}) = \varepsilon_{ij}^{\mathrm{PBC}}(\boldsymbol{x}) + \varepsilon_{ij}^0. \tag{38}$$

This means that the displacement field resulting from the same summation procedure has two spurious components, a linear one and a constant one:

$$u_i(\boldsymbol{x}) = u_i^{\mathrm{PBC}}(\boldsymbol{x}) + \boldsymbol{g}_i \cdot \boldsymbol{x} + u_i^0, \tag{39}$$

where u_i^{PBC} is the periodic displacement field, $\boldsymbol{g}_i$ and u_i^0 are a constant vector and a constant scalar, respectively. The constant field $\boldsymbol{\varepsilon}^0$, which must be subtracted from $\boldsymbol{\varepsilon}$, is deduced from $\boldsymbol{g}_i$:

$$\varepsilon_{ij}^0 = \frac{1}{2}(g_{ij} + g_{ji}). \tag{40}$$

The constant vector $\boldsymbol{g}_i$ can be computed by evaluating the displacement field (39) at one corner of the box and at the three adjacent corners. Although this method is simple and general, it is rather cumbersome in the present context, since with the FMM we only have access to the strain field. The evaluation of the displacement field would require to develop an additional FMM, which we want to avoid.

Recently it has been shown that for a box containing an elastic dipole component but no monopole term, the field $\boldsymbol{\varepsilon}^0$ can be written in the following explicit form [48]:

$$\varepsilon^0_{ij}(\boldsymbol{x}) = \frac{1}{2}\int_{\mathcal{S}} p_{lk} n_k \left[G^{\infty}_{il,j}(\bar{\boldsymbol{x}}) + G^{\infty}_{jl,i}(\bar{\boldsymbol{x}})\right] \mathrm{d}S', \tag{41}$$

where $\boldsymbol{p} = \boldsymbol{P}/V$, with $\boldsymbol{P}$ the elastic dipole tensor of the system and V the volume of the simulation box, $\boldsymbol{n}$ the outward-pointing normal to the integration surface $\mathcal{S}$. This surface delimits the domain over which the direct summation over strain sources is performed. Actually, since the function to integrate varies as $1/\bar{x}^2$, the integral does not depend on the domain itself, but only on its shape. The summation domain must be sufficiently large to fully account for higher order terms, which are absolutely convergent. In practice, using 2 to 3 macroscopic levels in FMM is enough. The field $\boldsymbol{\varepsilon}^0$ is calculated at the center of the simulation box. In isotropic elasticity, it is convenient to use the analytical form given in Ref. [48] and recalled in Appendix F.

Removing $\boldsymbol{\varepsilon}^0$ amounts to simulating a finite macroscopic system under loading given by $\boldsymbol{\sigma} = -\boldsymbol{p}$ [48]. This means that to simulate a physical system with free surfaces, this loading should be removed. Finally the strain in a macroscopic system with free surfaces is obtained from the FMM field $\boldsymbol{\varepsilon}^{\mathrm{FMM}}$ through

$$\boldsymbol{\varepsilon}(\boldsymbol{x}) = \boldsymbol{\varepsilon}^{\mathrm{FMM}}(\boldsymbol{x}) - \boldsymbol{\varepsilon}^0 + \boldsymbol{S}\boldsymbol{p}, \tag{42}$$

where $\boldsymbol{S}$ is the compliance matrix, *i.e.* the inverse of the stiffness matrix (see Eq. (6)):

$$S_{ijkl} = \frac{1}{4\mu}(\delta_{ik}\delta_{jl} + \delta_{il}\delta_{jk}) - \frac{\nu}{2\mu(1+\nu)}\delta_{ij}\delta_{kl}. \tag{43}$$

Tensor $\boldsymbol{p}$ remains to be determined. During the upward pass of the FMM, the multipole expansion of the field generated by all objects in the simulation box is calculated, so the strain field can be written as

$$\varepsilon_{ij}(\boldsymbol{x}) = \sum_{l=0}^{p}\sum_{m=-l}^{l} M^{ij,(0)}_{lm}\frac{Y^m_l(\theta,\varphi)}{x^{l+1}} + x^2\sum_{l=0}^{p}\sum_{m=-l}^{l} M^{ij,(2)}_{lm}\frac{Y^m_l(\theta,\varphi)}{x^{l+1}}. \tag{44}$$

Far from the simulation box, one must recover the strain field of an elastic dipole, decaying as $1/x^3$. This means that $M^{ij,(0)}_{2m}$ and $M^{ij,(2)}_{4m}$ are related to the total elastic dipole in the simulation box. The displacement field induced by an elastic dipole $\boldsymbol{P}$ located at the origin in the middle of the box is [49]

$$u^{\mathrm{dip}}_i(\boldsymbol{x}) = -G^{\infty}_{ij,k}(\boldsymbol{x})P_{jk} \tag{45}$$

$$= -\frac{1}{16\pi\mu(1-\nu)}\left[-2(1-2\nu)\frac{x_k}{x^3}P_{ik} + \frac{x_i}{x^3}\,\mathrm{Tr}\,(\boldsymbol{P}) - 3\frac{x_i x_k x_l}{x^5}P_{lk}\right], \tag{46}$$

from which the strain field is obtained:

$$\begin{aligned}\varepsilon_{ij}^{\mathrm{dip}}(\boldsymbol{x}) = -\frac{1}{16\pi\mu(1-\nu)}\Bigg[&-2(1-2\nu)\frac{P_{ij}}{x^3}\\ &+\frac{x^2\delta_{ij}-3x_ix_j}{x^5}\,\mathrm{Tr}\,(\boldsymbol{P})\\ &-6\nu\frac{x_i}{x^5}\,(x_kP_{jk})\\ &-6\nu\frac{x_j}{x^5}\,(x_kP_{ik})\\ &+3\frac{5x_ix_j-\delta_{ij}x^2}{x^7}x_kx_lP_{kl}\Bigg]. \quad (47)\end{aligned}$$

From this expression, one can evaluate the multipole expansion coefficients $M_{20}^{ij,(0)}$ (see Eq. (B.3))

$$M_{20}^{ij,(0)} = \int_0^{2\pi}\int_0^{\pi}\frac{5}{4\pi}\varepsilon_{ij}^{\mathrm{dip}}(\boldsymbol{x})x^3(Y_2^0(\theta,\varphi))^*\sin\theta\,\mathrm{d}\theta\mathrm{d}\varphi. \quad (48)$$

This leads to the following linear system:

$$M_{20}^{11,(0)} = \frac{1}{16\pi\mu(1-\nu)}\left[\frac{4}{7}(4-7\nu)P_{11}-\frac{4}{7}P_{22}+\frac{2}{7}P_{33}\right] \quad (49)$$

$$M_{20}^{22,(0)} = \frac{1}{16\pi\mu(1-\nu)}\left[-\frac{4}{7}P_{11}+\frac{4}{7}(4-7\nu)P_{22}+\frac{2}{7}P_{33}\right] \quad (50)$$

$$M_{20}^{33,(0)} = \frac{1}{16\pi\mu(1-\nu)}\left[\frac{2}{7}P_{11}+\frac{2}{7}P_{22}-\frac{8}{7}(4-7\nu)P_{33}\right] \quad (51)$$

$$M_{20}^{23,(0)} = -\frac{1}{16\pi\mu(1-\nu)}\frac{2}{7}(5-7\nu)P_{23} \quad (52)$$

$$M_{20}^{13,(0)} = -\frac{1}{16\pi\mu(1-\nu)}\frac{2}{7}(5-7\nu)P_{13} \quad (53)$$

$$M_{20}^{12,(0)} = \frac{1}{16\pi\mu(1-\nu)}\frac{4}{7}(5-7\nu)P_{12}. \quad (54)$$

This system is underdetermined for $\nu = 1/2$ or $\nu = 4/7$. In practice $\nu < 1/2$ so it can be safely used to calculate the dipole tensor associated to the simulation box and thus $\boldsymbol{p}$.

3.2. Free surfaces

The elastic Green function given in Eq. (5) is only valid for an infinite medium. If some boundaries of the simulation box correspond to a free surface, the strain field calculated with this Green function may be erroneous. Unphysical forces $\boldsymbol{T}$ may appear at the surface if some objects are too close to it. In order to obtain the correct elastic solution, we adopt the method proposed by van der Giessen and Needleman [50]. They add a field which cancels surface tractions produced by the solution in an infinite medium.

This field is the solution of the following equations:

$$\boldsymbol{\nabla} \cdot \boldsymbol{\sigma} = 0 \quad \text{in } \mathcal{V} \tag{55}$$

$$\boldsymbol{\sigma} \cdot \boldsymbol{n} = -\boldsymbol{T} \quad \text{on } \mathcal{S}^{\text{f}}, \tag{56}$$

where $\mathcal{V}$ is the domain corresponding to the simulation box, $\mathcal{S}^{\text{f}}$ its free surfaces, $\boldsymbol{n}$ is the outward normal vector to $\mathcal{S}^{\text{f}}$. Although surface tractions can vary steeply, the field induced by these forces smoothen with depth. An adaptive mesh is therefore particularly adapted to solve these equations. The finite element method (FEM) can be easily used with adaptive meshes, which makes this method particularly interesting in this context. It is based on the variational formulation of problem (55)-(56) [51]: we must find $\boldsymbol{u}$ such that

$$\int_{\mathcal{V}} \boldsymbol{\sigma}(\boldsymbol{u}) : \boldsymbol{\varepsilon}(\boldsymbol{v}) \, \mathrm{d}V = -\int_{\mathcal{S}^{\text{f}}} \boldsymbol{T} \cdot \boldsymbol{v} \, \mathrm{d}S \qquad \forall \boldsymbol{v} \in H^1, \tag{57}$$

with $\boldsymbol{u}$ the displacement field to be found, $\boldsymbol{v}$ a vector test function and H^1 the Sobolev space of vector functions. The colon operator is the inner product between two tensors, *i.e.* $\boldsymbol{\sigma} : \boldsymbol{\varepsilon} = \sigma_{ij}\varepsilon_{ij}$. Since there is no Dirichlet boundary condition (on $\boldsymbol{u}$), the solution is not unique. If free surfaces are considered in the three directions of space, *i.e.* with pure Neumann boundary conditions, any rigid body motion, given by (with $\boldsymbol{a}$, $\boldsymbol{b}$ constant vectors)

$$\boldsymbol{u}(\boldsymbol{x}) = \boldsymbol{a} \times \boldsymbol{x} + \boldsymbol{b}, \tag{58}$$

can be added to the solution ($\boldsymbol{\varepsilon}(\boldsymbol{u}) = 0$). The space of rigid body motions RM consists of translations and rotations, and for a pure Neumann problem, it is of dimension 6.

A unique solution can be found by setting the displacement of some points to zero [52]. Here we use Lagrange multipliers [51] to impose that the solution is linearly independent of functions in RM. This leads to the following saddle point problem [51, 53]: we must find $(\boldsymbol{u}, \boldsymbol{\lambda})$, with $\boldsymbol{u}$ in H^1 and $\boldsymbol{\lambda}$ in RM, such that

$$\int_{\mathcal{V}} \boldsymbol{\sigma}(\boldsymbol{u}) : \boldsymbol{\varepsilon}(\boldsymbol{v}) \, \mathrm{d}V + \int_{\mathcal{V}} \boldsymbol{v} \cdot \boldsymbol{\lambda} \, \mathrm{d}V = -\int_{\mathcal{S}^{\text{f}}} \boldsymbol{T} \cdot \boldsymbol{v} \, \mathrm{d}S \qquad \forall \boldsymbol{v} \in H^1 \tag{59}$$

$$\int_{\mathcal{V}} \boldsymbol{u} \cdot \boldsymbol{\mu} \, \mathrm{d}V = 0 \qquad \forall \boldsymbol{\mu} \in RM. \tag{60}$$

The number of rigid body motions to be blocked depends on the number of surfaces. The three translation motions must always be included in the rigid motions to be blocked; however the three rotations must be included only if the simulation box has free surfaces along the three directions of space. If PBCs are used along one direction, only the rotation around this direction must be blocked, so the null space of rigid body motions is of dimension 4. If PBCs are used along two directions, only translations must be considered and the null space is only of dimension 3. In practice, problem (59)-(60) was solved using the open-source software FEniCS [54].

The mesh to be used in FEM calculations can be fixed at the beginning of an OKMC simulation, but this is not always optimal in terms of efficiency and accuracy.

If strain sources remain far from surfaces, spatial variations of surface tractions are gentle and a coarse mesh can be used near surfaces without loss of accuracy, resulting in highly efficient FEM solving. If strain sources get closer to the surface as the simulation proceeds, surface tractions are expected to vary much more steeply and the mesh should be locally refined. Refining the mesh only where it is necessary is important to keep the FEM solving efficient. The adaptive FMM provides a rather natural way to do so. Since the FMM box size depends on the local density of sources, steep variations of the traction field resulting from sources close to the surface are expected to be accompanied with a local decrease of the FMM box size. Accordingly, we set the typical size of FEM elements at the surface proportional to the size of FMM boxes. In addition, the number of surface traction evaluations is set the same for all FMM boxes, resulting in a higher density of evaluations where FMM boxes are smaller. A schematical view of the FMM/FEM coupling is shown in Fig. 3.

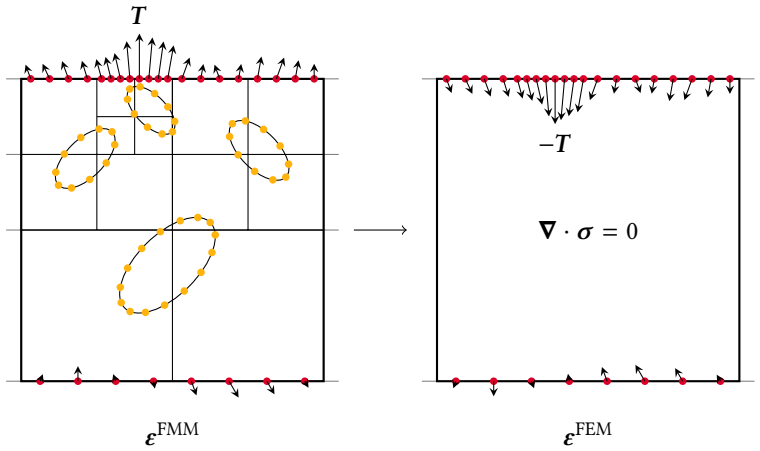

Figure 3. Coupling of adaptive FMM and FEM to obtain the solution compatible with traction-free upper and lower boundaries. The solution in an infinite medium is first obtained, using FMM ($\boldsymbol{\varepsilon}^{\mathrm{FMM}}$). The adaptive grid is used to evaluate traction forces $\boldsymbol{T}$ on surfaces. Then the solution at mechanical equilibrium under prescribed traction forces $-\boldsymbol{T}$ is determined with FEM ($\boldsymbol{\varepsilon}^{\mathrm{FEM}}$). The solution of the initial problem is $\boldsymbol{\varepsilon} = \boldsymbol{\varepsilon}^{\mathrm{FMM}} + \boldsymbol{\varepsilon}^{\mathrm{FEM}}$.

We chose the open-source software Gmsh [55] to generate the FEM mesh. This mesh is updated as infrequently as possible, only when the FMM adaptive mesh is modified. Otherwise, only surface tractions are re-evaluated before the FEM solving. Between two successive FEM solvings with the same mesh, the solutions are not expected to vary much and it is advantageous to re-use the solution from a preceding solving as an initial guess if an iterative solver is used. If a direct solver is employed, it is useful to re-use the LU factorization.

4. Numerical results

In this section we present a few test cases, to assess the accuracy and performance of the method, and to highlight its capabilities. All tests are performed in aluminum at room temperature. Parameters, which are taken from Ref. [13], are reminded in Table 1.

Table 1. Material parameters for aluminum

Parameter	Symbol	Value
Lattice parameter	a_0	0.405 nm
Atomic volume	Ω	$a_0^3/4 = 0.0167$ nm^3
Poisson's ratio	ν	0.35
Shear modulus	μ	26 GPa
Burgers vector (Frank loops)	$\boldsymbol{b}$	$a_0[111]/3$
Capture radius of dislocations	r_c	0.47 nm
Migration energy of vacancies	E_v^m	0.605 eV
Migration energy of SIAs	E_i^m	0.105 eV
Attempt frequency	ν_0	10^{13} Hz
Elastic dipole of vacancies at stable position	$\boldsymbol{P}_\mathrm{v}^\mathrm{e}$	$\begin{bmatrix} -3.238 & 0 & 0 \\ 0 & -3.238 & 0 \\ 0 & 0 & -3.238 \end{bmatrix}$ eV
Elastic dipole of vacancies at saddle position (jump in [110] direction)	$\boldsymbol{P}_\mathrm{v}^\mathrm{s}$	$\begin{bmatrix} -2.866 & -0.080 & 0 \\ -0.080 & -2.866 & 0 \\ 0 & 0 & 1.000 \end{bmatrix}$ eV
Elastic dipole of SIAs at stable position ([100] orientation)	$\boldsymbol{P}_\mathrm{i}^\mathrm{e}$	$\begin{bmatrix} 19.652 & 0 & 0 \\ 0 & 18.518 & 0 \\ 0 & 0 & 18.518 \end{bmatrix}$ eV
Elastic dipole of SIAs at saddle position (jump in [110] direction)	$\boldsymbol{P}_\mathrm{i}^\mathrm{s}$	$\begin{bmatrix} 19.498 & 1.133 & 0 \\ 1.133 & 19.498 & 0 \\ 0 & 0 & 19.034 \end{bmatrix}$ eV

4.1. Accuracy and performance of the method

The truncation of expansions to order p limits the accuracy of the method. The error on any component of the strain field can be conveniently estimated by the L^2 relative error norm [25, 39]:

$$e_2 = \left(\frac{\sum_{k=1}^{n} |\varepsilon^\mathrm{direct}(\boldsymbol{x}_k) - \varepsilon^\mathrm{FMM}(\boldsymbol{x}_k)|^2}{\sum_{k=1}^{n} |\varepsilon^\mathrm{direct}(\boldsymbol{x}_k)|^2} \right)^{1/2}, \tag{61}$$

where the indexes of the strain component have been dropped for the sake of clarity. The strain field component ε^FMM is calculated by FMM, with expansions truncated to order

p. A direct summation over all strain sources is performed to evaluate $\varepsilon^{\text{direct}}$, which is our reference value. The location of the n strain field evaluations (with $n = 10^4$ here) is chosen randomly in the matrix, outside the absorption region of sinks. In the test case considered here, sinks are Frank loops of the same radius, equal to 5 nm. Each loop is modelled as a collection of straight dislocation segments of maximum length equal to 1 nm. The absorption regions are cylinders of radius $r_c = 2b$, where $b = |\boldsymbol{b}|$, centered on the dislocation segments. A total of 40 loops, randomly placed in a cubic system of edge length 200 nm, generate the strain field. Neither periodic boundary conditions nor coupling with FEM are considered.

The relative error on ε_{11} is shown in Fig. 4 as a function of truncation order p. It steadily decreases with increasing order. Since the computation cost increases with p, its value should be chosen as small as possible. In general, a value of e_2 lower than 10^{-2} is unnecessary, so in the following $p = 7$ is adopted.

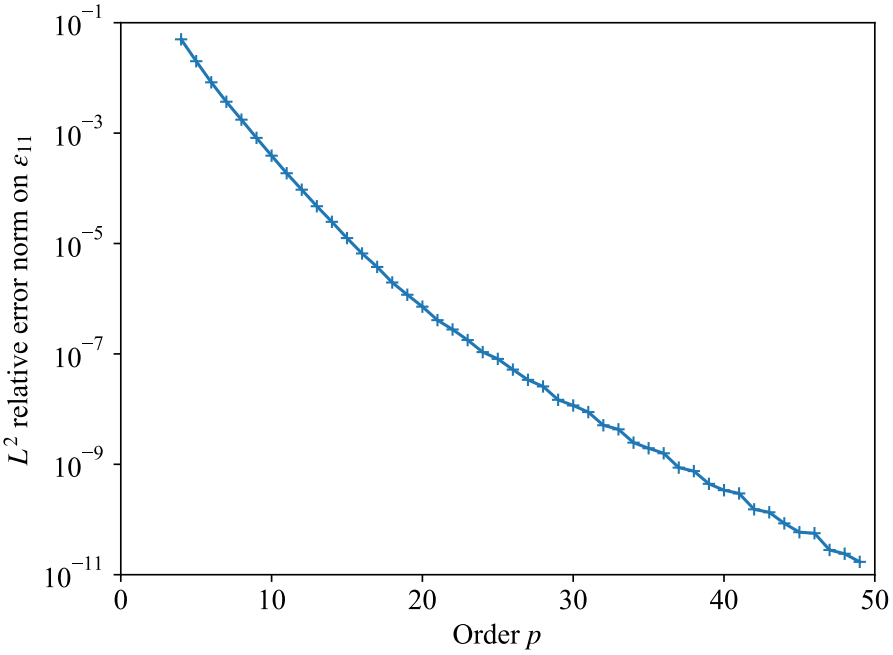

Figure 4. L^2 relative error norm on component ε_{11} as a function of the order p of the multipole and local expansions in the FMM. The system is cubic, of size 200 nm. It contains 40 Frank dislocation loops of 5 nm radius. The error is calculated on $n = 10^4$ points located outside the absorption region of loops.

The main purpose of using FMM is to reduce the computation time for the evaluation of the strain field. Computation times obtained with a direct calculation and with FMM, assuming that the expansions are up to date, are shown in Fig. 5-(a). The system is the same as before, but the number of loops, or equivalently the number of strain sources, is varied. The highest number of loops considered (100 loops) corresponds to loop densities typically seen in irradiated materials ($\sim 10^{22}$ m^{-3}). The computation

time with the direct approach increases linearly with the number of sources and reaches values of more than 10^{-3} s for 100 loops. When the FMM is used, the computation time is reduced by a factor of around 500 in this high density case. With the FMM, the field is calculated as the sum of two contributions. The first one includes sources which are sufficiently far from the box containing the target point. It is evaluated with a local expansion to order p. The associated computation time is independent of the number of sources. The second contribution is due to the remaining sources, which are too close to the box containing the target point to be included in the local expansion. In the adaptive FMM, they are taken into account with a multipole expansion if the box containing the sources is sufficiently far from the target and if it has a large number of sources. Otherwise, a direct summation on sources is performed (orange sources in Fig. 2). This second contribution explains the increase in computation time with the number of loops. If the maximum number of sources per box is reduced from 70 to 30, additional levels are introduced and in general, the number of sources which contribute to the direct sum decreases. That is why the computation time also decreases. The case of a uniform FMM, with a box size equal to 5 nm, is also reported in Fig. 5-(a). If the number of loops is small, boxes containing target points are most often surrounded by boxes with no sources. The computational cost corresponds to the evaluation of a local expansion. Once the number of loops is sufficiently large to populate the boxes around each target point, the computation time increases because of the direct summation.

As a first approximation, PBCs can be introduced in the direct approach by summing the contributions of sources located in the first neighbour shell of periodic images. This is not a bad approximation if PBCs are used along at most two directions, since the sum is absolutely convergent in this case (see Section 3.1). The computation time when PBCs are set along two directions corresponds to the dashed black line in Fig. 5-(a). As expected, it is around 9 times higher than without PBCs. With FMM, the computation time only marginally increases, because the number of sources on which the direct summation is performed only increases for target points located close to the boundaries of the system. This is a clear advantage of the FMM over the direct calculation.

Up to now it has been assumed that multipole and local expansions are up to date. Each time a sink absorbs or emits a point defect, expansions must be updated. We see in Fig. 5-(b) that with our version of the FMM, which is not fully optimized, the calculation of multipole and local expansions for all strain components can be up to a few seconds for dense microstructures. It increases if $n_{\max}$ decreases, since additional levels are introduced. We have seen that on the contrary, reducing $n_{\max}$ speeds up the field evaluation. So $n_{\max}$ must be adjusted to minimize the sum of the two contributions to the computation time. Empirically, $n_{\max} = 70$ appears to be satisfactory with the present implementation. We also see in Fig. 5-(b) that considering PBCs hardly affects the time to update expansions, so that the global computation time is nearly independent of PBCs with FMM. As in Fig. 5-(a), the computation time for the uniform FMM is reported. With such a small box size of 5 nm, the update of expansions takes

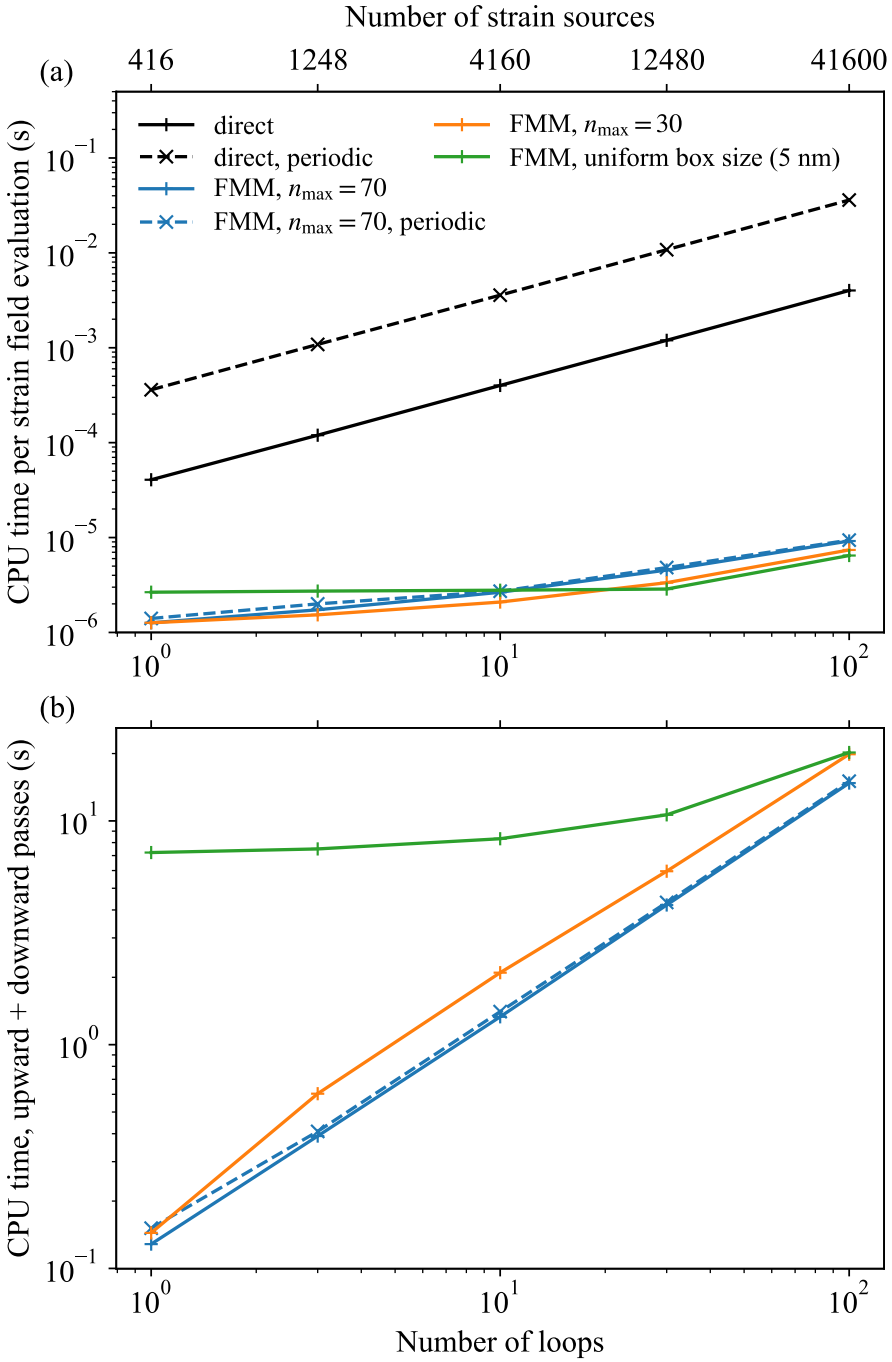

Figure 5. (a) Computation time for one strain field evaluation, for direct and FMM calculations, as a function of the number of loops in a $(200\ \text{nm})^3$ system. Loops have a radius of 5 nm. Dashed curves refer to periodic calculations along two directions. Periodic images are only partially accounted for in the direct calculation, by including the first neighbour shell (8 images boxes). The adaptive version of the FMM is used with two different criteria for the division of boxes ($n_{\text{max}} = 30$ and $n_{\text{max}} = 70$). The green curve corresponds to a FMM calculation with a 5 nm uniform mesh. (b) Computation time for the initial evaluation of local expansions by FMM.

much more time than with the adaptive FMM. Although the box size can be tuned to obtain satisfactory performance, it becomes difficult to do so when the number of sources evolves appreciably with time. This is typically the case under irradiation, with the nucleation and growth of clusters. So in general the adaptive version should be preferred.

Since the update of FMM expansions takes significant time, the FMM is useful only if defects perform a large number of jumps n between two absorption or emission events. The speed-up is then

$$s = \frac{(z+1)nt_{\text{direct}}}{(z+1)nt_{\text{FMM}} + t_{\text{update}}}, \tag{62}$$

where t_{direct} and t_{FMM} are the computation time per evaluation of strain field (Fig. 5-(a)) in the direct and FMM approaches, respectively, and t_{update} is the time required to update FMM expansion coefficients (Fig 5-(b)). The factor $(z+1)$ accounts for the z possible jumps a defect can perform (8 for an SIA, 12 for a vacancy), because an estimation of the field is necessary for each saddle point. In addition the interaction energy for the initial stable configuration must be calculated. To evaluate n, let us consider absorption events only and neglect elastic interactions. The average number of jumps of a defect before absorption is [56]

$$n = \frac{12}{k^2 a_0^2}, \tag{63}$$

where the sink strength is assumed to be the one of a concentration C of loops of radius r and capture radius r_{c} [57]:

$$k^2 = \frac{4\pi^2 r}{\ln\left(\frac{8r}{r_{\text{c}}}\right)} C. \tag{64}$$

For one loop in the simulation box, we obtain around $n = 10^7$ jumps before absorption, while for 100 loops, n is around 10^5. From results shown in Fig. 5, the resulting speed-up for a system with PBCs in two directions is around 250 for one loop and 1700 for 100 loops. The proportion of time taken for the update of FMM expansion coefficients increases with the number of loops, so that $(z+1)nt_{\text{FMM}} \approx t_{\text{update}}$ for 100 loops. However, the time for direct evaluation of the field also increases rapidly with the number of loops. This results in a larger speed-up if the number of loops increases.

A more precise estimation of the speed-up is obtained by measuring the average CPU time per KMC time step directly in a kinetic simulation. This measurement also takes into account a variety of other operations occurring during a KMC time step, such as the computation of energy, the handling of collisions between defects, etc. Previous microstructures are taken as starting configurations. They evolve following the creation of Frenkel pairs at a rate of 10^{-4} dpa/s. Results are shown in Fig. 6. The speed-up is similar to the previous estimation, from two to three orders of magnitude depending on the number of loops in the system. As before, the update of FMM expansion coefficients takes a larger proportion of the computation time as the number of loops increases. We

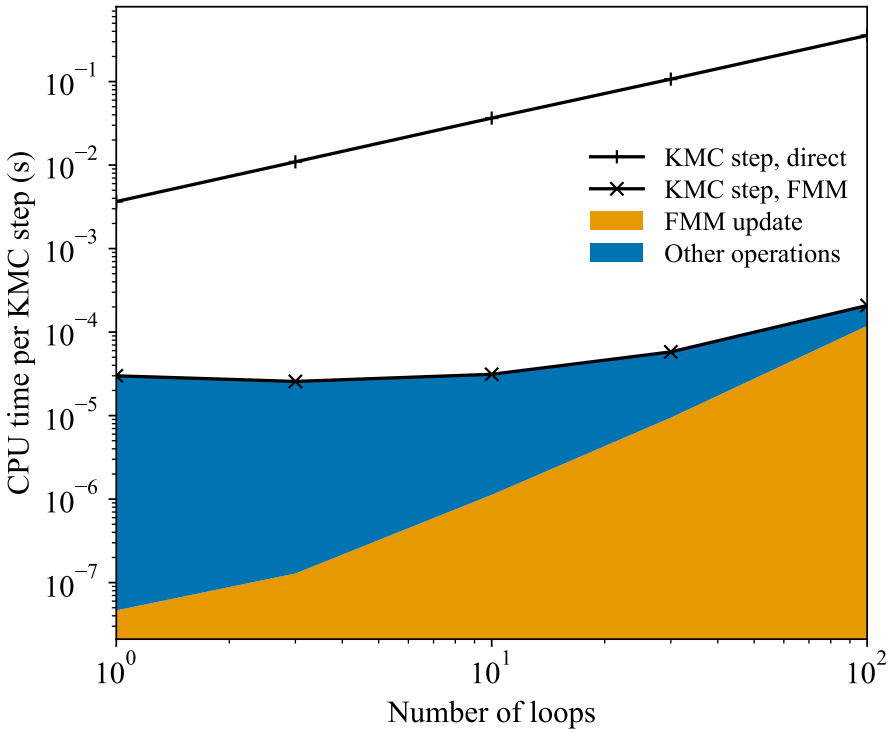

Figure 6. Computation time per KMC step as a function of the number of loops in a $(200\ \text{nm})^3$ system. Loops have a radius of 5 nm. Direct and FMM calculation of the strain field are shown in black solid lines. For FMM, the orange colour area indicates the proportion of time spent in the update of FMM expansion coefficients, other operations being represented in blue.

note that in these simulations, we avoid recalculating all multipole expansion coefficients each time an absorption event occurs. Only boxes whose sources have changed have their multipole expansions updated. Then only necessary multipole-to-local operations are performed, which saves computation time.

4.2. Impact of free surface on dislocation loop growth

In the vicinity of a surface, the growth rate of clusters is altered, because a proportion of point defects is absorbed by this sink instead of contributing to cluster evolution. This leads, for example, to the presence of void and loop denuded zones [58, 59, 60]. This effect has been investigated with standard OKMC [61]. With the present method it is possible to study a more subtle effect, related to the strain field generated by clusters. We have seen in section 3.2 that if a cluster is located close to a surface, the associated strain field does not correspond to the field generated in an infinite medium, since surfaces must be traction-free. The resulting modified energy landscape impacts the diffusion paths of point defects and thus may change the cluster behaviour.

In the following we consider a system with free surfaces along $\boldsymbol{e}_3$, containing a loop

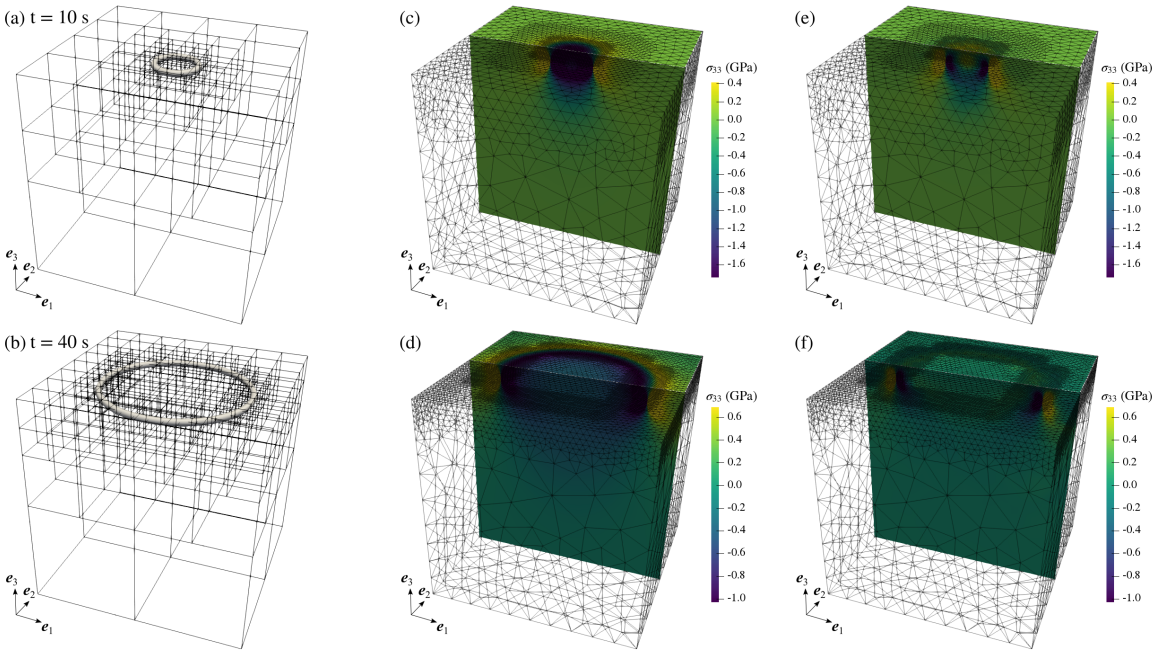

Figure 7. Visualization of the computation of the strain field produced by a dislocation loop located at 2 nm from the upper surface of a $(30\ \text{nm})^3$ system, at (a,c,e) $t = 10$ s and (b,d,f) $t = 40$ s. (a,b) Adaptive FMM mesh. (c,d) Component σ_{33} induced by the presence of the loop, if the solution in an infinite medium is used. This solution leads to significant traction forces $\boldsymbol{T}$ on the upper surface. (e,f) Component σ_{33} when the FEM solution of the mechanical equilibrium with prescribed forces $-\boldsymbol{T}$ is added to the infinite medium solution.

nucleus at a variable distance d from the upper surface. PBCs are used in the two other directions. The loop nucleus is an interstitial cluster containing 11 SIAs ($r = 0.5$ nm), which is assumed to be immobile and to grow as a Frank loop oriented parallel to the surface. The dimensions of the system are 30 nm $\times$ 30 nm $\times$ 30 nm. SIAs and vacancies are inserted as Frenkel pairs at a dose rate of 5×10^{-3} dpa/s. A view of the FMM adaptive mesh at two different times is given in Fig. 7-(a,b). The region where the mesh is refined correlates with the position of the dislocation line. Following the coupling scheme proposed in Fig. 3, this mesh refinement leads to a fine FEM mesh at the upper surface close to the dislocation line, where the field varies steeply (Fig. 7-(c,d)). In the case shown in Fig. 7, which corresponds to a dislocation loop 2 nm away from the upper surface, traction forces created by the solution in a infinite medium can be larger than 1 GPa. When the FEM solution of the mechanical equilibrium with opposite traction forces is added, traction forces are substantially reduced. We see that this induces a significant change in the stress inside the material (Fig. 7-(e,f)).

The evolution of loop size with time is shown in Fig. 8, including or not the compensation of traction forces. 20 simulations have been performed for distances to the surface ranging from 2 to 15 nm. One sees that except when the loop is very close to the surface ($d = 2$ nm), the image field correction has only a small influence on loop growth.

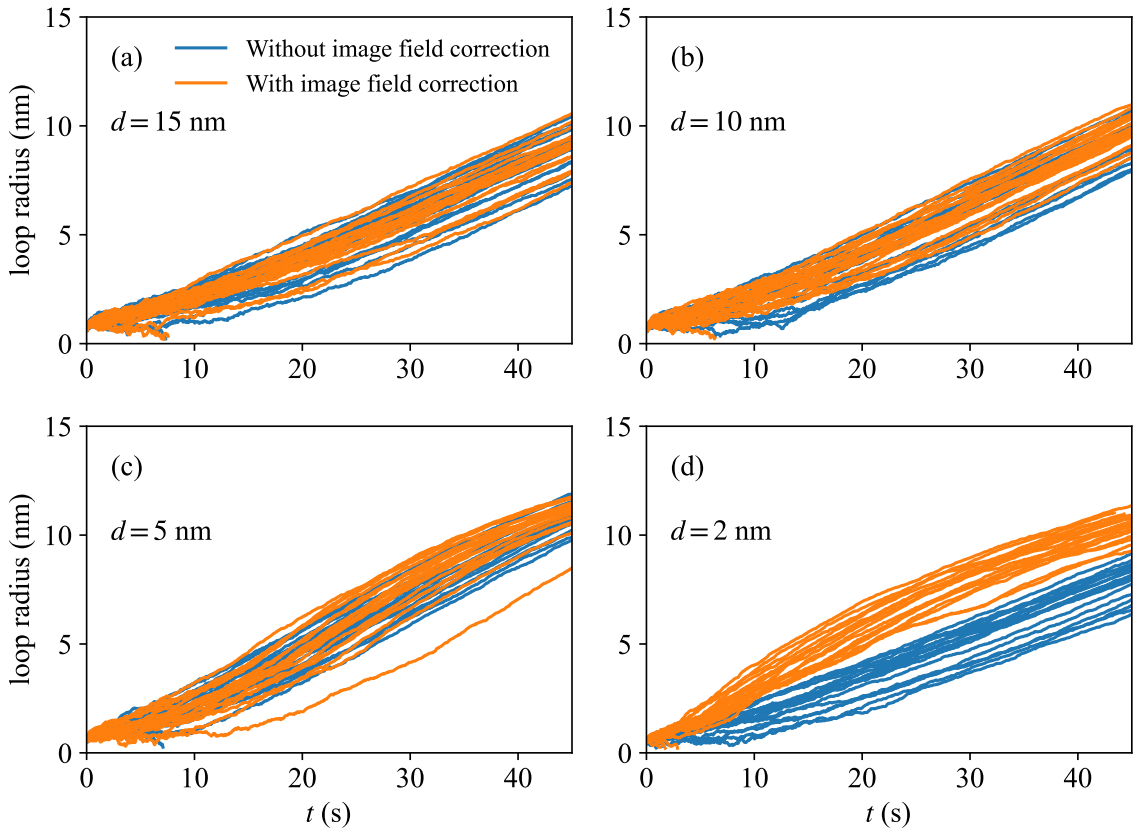

Figure 8. Evolution of loop radius with time for different distances to the surface d. 20 simulations have been performed for each value of d, with and without compensation of traction forces created by the elastic solution in an infinite medium.

4.3. Evolution of dislocation loops in thin foils under irradiation

It is known that in thin foils of fcc and bcc metals, interstitial dislocation loops grow under irradiation [62, 63]. This growth is explained successfully by the so-called "dislocation bias model" [2]. Loops interact more strongly with SIAs than vacancies, which results in a preferential absorption of SIAs. The remaining net quantity of vacancies in the matrix is absorbed by sinks which generate shorter range, or less intense, elastic fields. These sinks can be cavities, surfaces or grain boundaries for example. However, shrinkage of interstitial dislocation loops has been observed in some cases under irradiation. In aluminum, it has been documented by Jitsukawa and Hojou in 600 nm thick foils irradiated in a transmission electron microscope [64]. These authors have explained loop shrinkage by a dependency of the elastic bias of loops on their size. Indeed, even though all loops have a positive elastic bias, which means they interact more strongly with SIAs than vacancies, it does not imply that they all grow. Since vacancies and SIAs are produced in equal quantities, loops with the smallest elastic bias necessarily absorb more vacancies than SIAs if no sinks with lower elastic bias are present (for example, surfaces). In general, small loops tend to exhibit lower growth

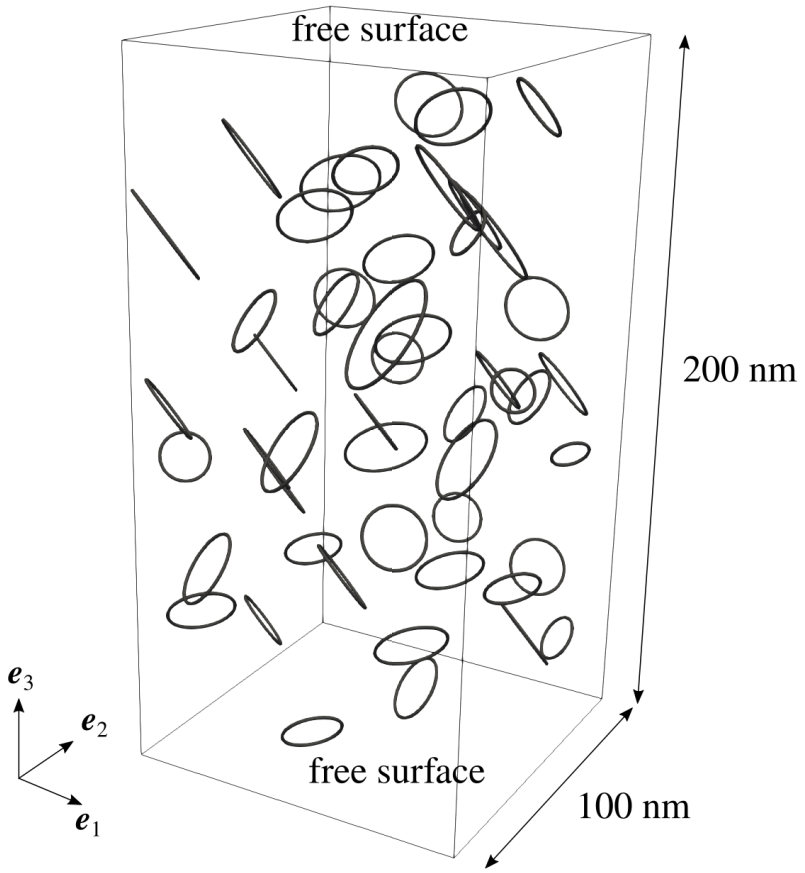

Figure 9. One of the 10 loop configurations considered to investigate loop growth dependency on distance to surface and loop radius.

rates than large loops, which points to an increase of the elastic bias with size. Numerical evaluations of bias of isolated loops are consistent with these findings [65, 66, 67].

Absorption efficiencies of loops depend not only on their size, but also on the surrounding microstructure [17, 16]. To assess more precisely the effect of elastic bias on loop behaviour, we simulate microstructures containing several loops of various sizes. We consider a system of size 100 nm $\times$ 100 nm $\times$ 200 nm, with free surfaces along $\boldsymbol{e}_3$ and PBCs in the two other directions. 50 dislocation loops are randomly placed in the simulation box, which represents a loop density of 2.5×20^{22} m^{-3}. Their radius is drawn from a normal distribution of mean 10 nm and of standard deviation 2 nm, and their habit plane is chosen randomly among the four possible ones. A total of 10 loop configurations are generated. Each configuration is simulated 5 times, with different random seeds, and the average growth rate of a loop is deduced from linear fits of the evolution of loop radius over 10 seconds. SIAs and vacancies are produced as Frenkel pairs, at a dose rate of 10^{-4} dpa/s. An example of a loop microstructure is shown in Fig. 9. No other sinks, such as cavities or grain boundaries, are introduced in the simulation.

Loop growth rate has a clear dependency on the distance of the loop to the surface d (Fig. 10-(a)). On average, loops close to the surface have the highest growth rate, because vacancies can easily reach the surface. For values of d larger than around 40 nm, surface effects become negligible. Vacancies are mostly absorbed by loops, which results in slow growth and even shrinkage of loops. The growth rate is plotted as a function of the loop radius in Fig. 10-(b), for loops which are more than 40 nm away from both surfaces. On average, the growth rate increases with the loop radius, although values are very scattered. This result is consistent with experiments and with the bias calculations on isolated loops, which show a strong increase of bias for small radii and a plateau at around 10 nm [66, 67]. The large scattering of growth rates points to an additional effect of the surrounding microstructure on the loop behaviour. Recently, it has been shown that to first order, the absorption efficiency of a loop is proportional to $(V/\bar{V})^{1/4}$, where V is the Voronoi volume of the loop and $\bar{V}$ is the average Voronoi volume [16]. The growth rate also seems to follow this trend (Fig. 10-(c)). The scattering is however large, which highlights the complex dependency of loop growth rate on the surrounding microstructure, especially when long range elastic interactions are taken into account. If other microstructural features with lower elastic bias, such as cavities, are present in sufficient number in the bulk, loop growth rates are expected to become all positive but still scattered.

Conclusion

A method has been proposed to efficiently and accurately estimate the strain field generated by defects in irradiated microstructures, in the framework of OKMC simulations. The strain field of cavities and dislocation segments is evaluated by a local expansion in spherical harmonics if the sources are sufficiently far from the evaluation point. Otherwise, a direct sum over the strain sources is performed. This leads to a drastic reduction in the evaluation time of the field compared to a direct summation over strain sources, especially if periodic boundary conditions are used.

To evaluate efficiently the local expansion coefficients, the FMM for biharmonic kernels, which relies on two calls to FMM for harmonic kernels, is used. The number of FMM calls is reduced with respect to previous approaches and kept independent on the number of field types (cavities, dislocation segments). These improvements could be interesting for other simulation methods which rely on FMM on biharmonic kernels, such as DDD.

In addition to its efficiency, another advantage of FMM is the relatively straightforward treatment of finite systems. If surfaces are located far away in the three directions of space and if the strain field contains a dipolar component, the sum of strain contributions over periodic images is conditionally convergent. The correction to this sum to give a system free from surface tractions is easily obtained from the multipole expansion of the system, which is a by-product of FMM. This situation is quite common in practice: it arises, for example, when the microstructure contains dislocation loops

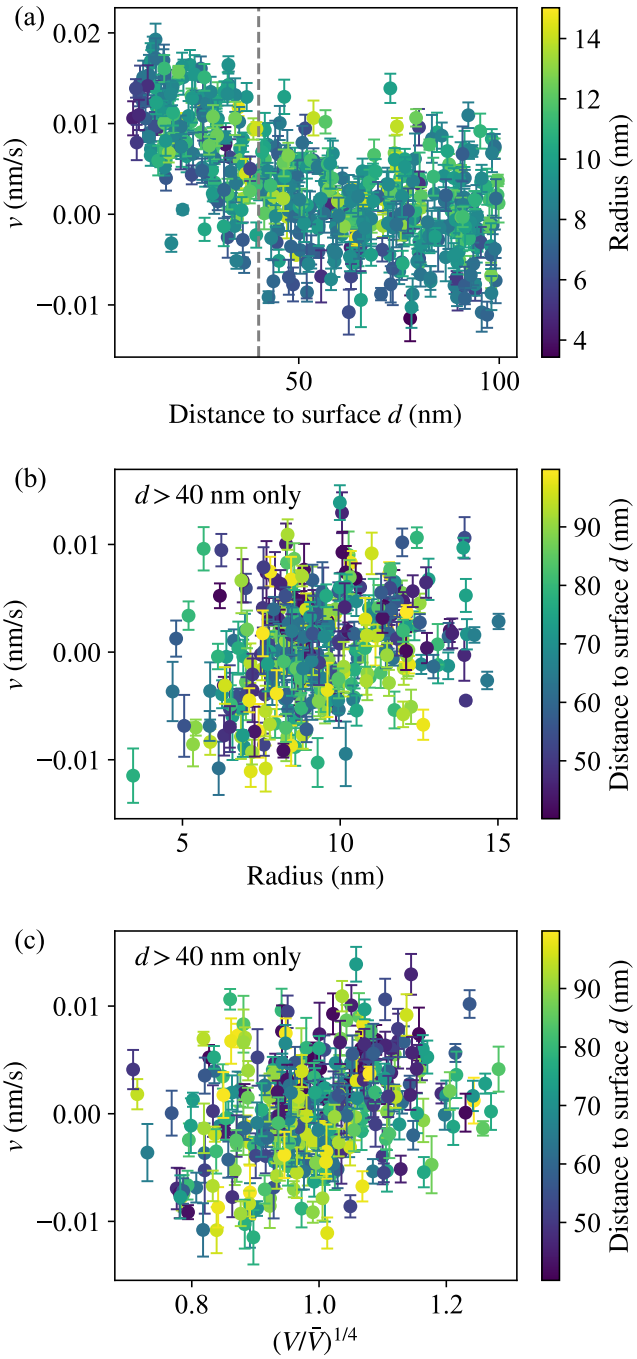

Figure 10. Loop growth rate in a 200 nm thick aluminum foil, irradiated at 10^{-4} dpa/s at 300 K. The system size is 100 nm in the two other directions. 10 loop configurations are simulated. Initial configurations contain a random arrangement of 50 loops, which corresponds to a density of 2.5×20^{22} m^{-3}. The loop radius is chosen randomly from a gaussian distribution of mean value 10 nm and of standard deviation 2 nm. Error bars correspond to the standard error of the mean calculated on 5 independent simulations of the same configuration. (a) Loop growth rate as a function of the distance of the loop to the closest surface d. (b) Loop growth rate as a function of the loop radius. Only loops which are more than 40 nm away from both surfaces are shown. (c) Loop growth rate as a function of $(V/\bar{V})^{1/4}$, where V is the Voronoi volume of the loop and $\bar{V}$ is the average Voronoi volume.

and cavities. If some surfaces correspond to the boundaries of the simulation box, an elastic problem with prescribed tractions on some of the boundaries must be solved with FEM. The adaptive mesh of the FMM is particularly convenient to build a FEM mesh fitting the variations of traction forces.

Preliminary simulations of loop microstructures with elastic interactions reveal the large scattering of loop growth rates, although correlations with loop radius and with the Voronoi volume of loops have been highlighted. These results show that using elastic bias of isolated defects is probably not sufficient to provide a quantitative description of irradiated microstructures.

Acknowledgments

This work has been carried out partly within the framework of the EUROfusion Consortium and has received funding from the Euratom research and training program under grant agreements No 633053 and 101052200 – EUROfusion. Views and opinions expressed are however those of the author only and do not necessarily reflect those of the European Union or the European Commission. Neither the European Union nor the European Commission can be held responsible for them.

Appendix A. Strain components for a dislocation loop

Using the notations from Section 1.2.1, explicit expressions of the strain components for a dislocation loop are (the dependency on v_α is dropped for clarity):

$$\begin{aligned}\varepsilon_{11}(\bar{\boldsymbol{x}}) = \frac{1}{8\pi}\sum_{\alpha=1}^{N_\mathrm{q}} w_\alpha \Bigg[& \frac{1}{1-\nu}\left(b_3\bar{x}_{,112} - b_2\bar{x}_{,113}\right) x'_{1,v} \\ & + \left(\frac{\nu}{1-\nu}b_1\bar{x}_{,113} - b_1\bar{x}_{,223} - b_1\bar{x}_{,333} - \frac{\nu}{1-\nu}b_3\bar{x}_{,111} + b_3\bar{x}_{,221} + b_3\bar{x}_{,331}\right) x'_{2,v} \\ & + \left(-\frac{\nu}{1-\nu}b_1\bar{x}_{,112} + b_1\bar{x}_{,222} + b_1\bar{x}_{,332} + \frac{\nu}{1-\nu}b_2\bar{x}_{,111} - b_2\bar{x}_{,221} - b_2\bar{x}_{,331}\right) x'_{3,v}\Bigg] \end{aligned} \quad \text{(A.1)}$$

$$\begin{aligned}\varepsilon_{22}(\bar{\boldsymbol{x}}) = \frac{1}{8\pi}\sum_{\alpha=1}^{N_\mathrm{q}} w_\alpha \Bigg[& \left(-\frac{\nu}{1-\nu}b_2\bar{x}_{,223} + b_2\bar{x}_{,333} + b_2\bar{x}_{,113} + \frac{\nu}{1-\nu}b_3\bar{x}_{,222} - b_3\bar{x}_{,332} - b_3\bar{x}_{,112}\right) x'_{1,v} \\ & + \frac{1}{1-\nu}\left(b_1\bar{x}_{,223} - b_3\bar{x}_{,221}\right) x'_{2,v} \\ & + \left(\frac{\nu}{1-\nu}b_2\bar{x}_{,211} - b_2\bar{x}_{,331} - b_2\bar{x}_{,111} - \frac{\nu}{1-\nu}b_1\bar{x}_{,222} + b_1\bar{x}_{,332} + b_1\bar{x}_{,112}\right) x'_{3,v}\Bigg] \end{aligned} \quad \text{(A.2)}$$

$$\varepsilon_{33}(\bar{\boldsymbol{x}}) = \frac{1}{8\pi}\sum_{\alpha=1}^{N_\mathrm{q}} w_\alpha \left[\left(\frac{\nu}{1-\nu}b_3\bar{x}_{,332} - b_3\bar{x}_{,112} - b_3\bar{x}_{,222} - \frac{\nu}{1-\nu}b_2\bar{x}_{,333} + b_2\bar{x}_{,113} + b_2\bar{x}_{,223}\right)x'_{1,v} + \left(-\frac{\nu}{1-\nu}b_3\bar{x}_{,331} + b_3\bar{x}_{,111} + b_3\bar{x}_{,221} + \frac{\nu}{1-\nu}b_1\bar{x}_{,333} - b_1\bar{x}_{,113} - b_1\bar{x}_{,223}\right)x'_{2,v} + \frac{1}{1-\nu}\left(b_2\bar{x}_{,331} - b_1\bar{x}_{,332}\right)x'_{3,v}\right] \quad \text{(A.3)}$$

$$\varepsilon_{23}(\bar{\boldsymbol{x}}) = \frac{1}{8\pi}\sum_{\alpha=1}^{N_\mathrm{q}} w_\alpha \left[\frac{1}{1-\nu}\left(b_3\bar{x}_{,223} - b_2\bar{x}_{,332}\right)x'_{1,v} + \frac{1}{2}\left(b_2\bar{x}_{,111} + b_2\bar{x}_{,221} + b_2\bar{x}_{,331} - b_1\bar{x}_{,112} - b_1\bar{x}_{,222} + \frac{1+\nu}{1-\nu}b_1\bar{x}_{,332} - \frac{2}{1-\nu}b_3\bar{x}_{,123}\right)x'_{2,v} + \frac{1}{2}\left(-b_3\bar{x}_{,111} - b_3\bar{x}_{,221} - b_3\bar{x}_{,331} + b_1\bar{x}_{,113} - \frac{1+\nu}{1-\nu}b_1\bar{x}_{,223} + b_1\bar{x}_{,333} + \frac{2}{1-\nu}b_2\bar{x}_{,123}\right)x'_{3,v}\right] \quad \text{(A.4)}$$

$$\varepsilon_{13}(\bar{\boldsymbol{x}}) = \frac{1}{8\pi}\sum_{\alpha=1}^{N_\mathrm{q}} w_\alpha \left[\frac{1}{2}\left(-b_1\bar{x}_{,222} - b_1\bar{x}_{,332} - b_1\bar{x}_{,112} + b_2\bar{x}_{,221} - \frac{1+\nu}{1-\nu}b_2\bar{x}_{,331} + b_2\bar{x}_{,111} + \frac{2}{1-\nu}b_3\bar{x}_{,123}\right)x'_{1,v} + \frac{1}{1-\nu}\left(b_1\bar{x}_{,331} - b_3\bar{x}_{,113}\right)x'_{2,v} + \frac{1}{2}\left(b_3\bar{x}_{,222} + b_3\bar{x}_{,332} + b_3\bar{x}_{,112} - b_2\bar{x}_{,223} - b_2\bar{x}_{,333} + \frac{1+\nu}{1-\nu}b_2\bar{x}_{,113} - \frac{2}{1-\nu}b_1\bar{x}_{,123}\right)x'_{3,v}\right] \quad \text{(A.5)}$$

$$\varepsilon_{12}(\bar{\boldsymbol{x}}) = \frac{1}{8\pi}\sum_{\alpha=1}^{N_\mathrm{q}} w_\alpha \left[\frac{1}{2}\left(b_1\bar{x}_{,333} + b_1\bar{x}_{,113} + b_1\bar{x}_{,223} - b_3\bar{x}_{,331} - b_3\bar{x}_{,111} + \frac{1+\nu}{1-\nu}b_3\bar{x}_{,221} - \frac{2}{1-\nu}b_2\bar{x}_{,123}\right)x'_{1,v} + \frac{1}{2}\left(-b_2\bar{x}_{,333} - b_2\bar{x}_{,113} - b_2\bar{x}_{,223} + b_3\bar{x}_{,332} - \frac{1+\nu}{1-\nu}b_3\bar{x}_{,112} + b_3\bar{x}_{,222} + \frac{2}{1-\nu}b_1\bar{x}_{,123}\right)x'_{2,v} + \frac{1}{1-\nu}\left(b_2\bar{x}_{,112} - b_1\bar{x}_{,221}\right)x'_{3,v}\right]. \quad \text{(A.6)}$$

Expressions of $\bar{x}_{,ijk}$ are given, for example, in Ref. [34].

Appendix B. Definition of spherical harmonics, solid harmonics and recursion formulas

The definition of spherical harmonics used here is the same as in Ref. [24]:

$$Y_l^m(\theta,\varphi) = \sqrt{\frac{(l-|m|)!}{(l+|m|)!}}P_l^{|m|}(\cos\theta)e^{im\varphi}, \quad \text{(B.1)}$$

where P_l^m are the associated Legendre polynomials, which are defined by

$$P_l^m(x) = (-1)^m (1-x^2)^{m/2} \frac{\mathrm{d}^m}{\mathrm{d}x^m} P_l(x). \tag{B.2}$$

In Eq. (B.2), P_l are the Legendre polynomials. From Eq. (B.1) we deduce that $(Y_l^m(\theta,\varphi))^* = Y_l^{-m}(\theta,\varphi)$. The normalisation is such that

$$\int_0^{2\pi} \int_0^{\pi} Y_l^m(\theta,\varphi)(Y_{l'}^{m'}(\theta,\varphi))^* \sin\theta \,\mathrm{d}\theta \mathrm{d}\varphi = \frac{4\pi}{2l+1} \delta_{ll'} \delta_{mm'}. \tag{B.3}$$

For example we have:

$$Y_1^0(\theta,\varphi) = \cos\theta \tag{B.4}$$

$$Y_1^1(\theta,\varphi) = -\frac{1}{\sqrt{2}} \sin\theta e^{i\varphi}. \tag{B.5}$$

Regular solid harmonics are defined by $R_l^m(x,\theta,\varphi) = x^l Y_l^m(\theta,\varphi)$ and irregular solid harmonics are defined by $I_l^m(x,\theta,\varphi) = Y_l^m(\theta,\varphi)/x^{l+1}$. Irregular solid harmonics can also be written as [68, 27]

$$I_l^m(x,\theta,\varphi) = (-1)^m A_l^m \left(\frac{\partial}{\partial x_1} + i\frac{\partial}{\partial x_2}\right)^m \left(\frac{\partial}{\partial x_3}\right)^{l-m} \left(\frac{1}{x}\right), \tag{B.6}$$

with

$$A_l^m = \frac{(-1)^l}{\sqrt{(l-m)!(l+m)!}} \tag{B.7}$$

(the factor $(-1)^m$ in Eq. (B.6) is missing in [27]).

We note

$$B_l^m = \sqrt{(l+m)(l-m)}, \tag{B.8}$$

$$C_l^m = \sqrt{(l+m)(l+m-1)}, \tag{B.9}$$

and

$$s(m) = \begin{cases} 1 & \text{if } m \geq 0 \\ -1 & \text{if } m < 0. \end{cases} \tag{B.10}$$

We can write recursion formulas under the form:

$$B_{l+1}^m Y_{l+1}^m - (2l+1) Y_1^0 Y_l^m + B_l^m Y_{l-1}^m = 0 \tag{B.11}$$

$$s(m-1) C_{l+1}^{-m+1} Y_{l+1}^{m-1} + \sqrt{2}(2l+1) Y_1^{-1} Y_l^m - s(m-1) C_l^m Y_{l-1}^{m-1} = 0 \tag{B.12}$$

$$s(m) C_{l+2}^m Y_{l+1}^{m+1} - \sqrt{2}(2l+1) Y_1^1 Y_l^m - s(m) C_l^{-m} Y_{l-1}^{m+1} = 0. \tag{B.13}$$

Using these formulas, it can be shown that products $x_k I_l^m(x,\theta,\varphi)$ can be decomposed as functions of $I_p^q(x,\theta,\varphi)$ and $x^2 I_p^q(x,\theta,\varphi)$:

$$\begin{aligned} x_1 I_l^m(x,\theta,\varphi) = &-\frac{1}{2(2l+1)} s(m) C_{l+2}^m x^2 I_{l+1}^{m+1}(x,\theta,\varphi) \\ &+ \frac{1}{2(2l+1)} s(m-1) C_{l+1}^{-m+1} x^2 I_{l+1}^{m-1}(x,\theta,\varphi) \\ &+ \frac{1}{2(2l+1)} s(m) C_l^{-m} I_{l-1}^{m+1}(x,\theta,\varphi) \\ &- \frac{1}{2(2l+1)} s(m-1) C_l^m I_{l-1}^{m-1}(x,\theta,\varphi) \end{aligned} \quad \text{(B.14)}$$

$$\begin{aligned} x_2 I_l^m(x,\theta,\varphi) = &\frac{i}{2(2l+1)} s(m-1) C_{l+1}^{-m+1} x^2 I_{l+1}^{m-1}(x,\theta,\varphi) \\ &+ \frac{i}{2(2l+1)} s(m) C_{l+2}^m x^2 I_{l+1}^{m+1}(x,\theta,\varphi) \\ &- \frac{i}{2(2l+1)} s(m) C_l^{-m} I_{l-1}^{m+1}(x,\theta,\varphi) \\ &- \frac{i}{2(2l+1)} s(m-1) C_l^m I_{l-1}^{m-1}(x,\theta,\varphi) \end{aligned} \quad \text{(B.15)}$$

$$x_3 I_l^m(x,\theta,\varphi) = \frac{B_{l+1}^m}{2l+1} x^2 I_{l+1}^m(x,\theta,\varphi) + \frac{B_l^m}{2l+1} I_{l-1}^m(x,\theta,\varphi). \quad \text{(B.16)}$$

Similar expressions can be deduced for $x_k R_l^m(x,\theta,\varphi)$, using Eqs (B.14)–(B.16) and the relation $R_l^m(x,\theta,\varphi) = x^{2l+1} I_l^m(x,\theta,\varphi)$:

$$\begin{aligned} x_1 R_l^m(x,\theta,\varphi) = &-\frac{1}{2(2l+1)} s(m) C_{l+2}^m R_{l+1}^{m+1}(x,\theta,\varphi) \\ &+ \frac{1}{2(2l+1)} s(m-1) C_{l+1}^{-m+1} R_{l+1}^{m-1}(x,\theta,\varphi) \\ &+ \frac{1}{2(2l+1)} s(m) C_l^{-m} x^2 R_{l-1}^{m+1}(x,\theta,\varphi) \\ &- \frac{1}{2(2l+1)} s(m-1) C_l^m x^2 R_{l-1}^{m-1}(x,\theta,\varphi) \end{aligned} \quad \text{(B.17)}$$

$$\begin{aligned} x_2 R_l^m(x,\theta,\varphi) = &\frac{i}{2(2l+1)} s(m) C_{l+2}^m R_{l+1}^{m+1}(x,\theta,\varphi) \\ &+ \frac{i}{2(2l+1)} s(m-1) C_{l+1}^{-m+1} R_{l+1}^{m-1}(x,\theta,\varphi) \\ &- \frac{i}{2(2l+1)} s(m) C_l^{-m} x^2 R_{l-1}^{m+1}(x,\theta,\varphi) \\ &- \frac{i}{2(2l+1)} s(m-1) C_l^m x^2 R_{l-1}^{m-1}(x,\theta,\varphi) \end{aligned} \quad \text{(B.18)}$$

$$x_3 R_l^m(x,\theta,\varphi) = \frac{B_{l+1}^m}{2l+1} R_{l+1}^m(x,\theta,\varphi) + \frac{B_l^m}{2l+1} x^2 R_{l-1}^m(x,\theta,\varphi). \quad \text{(B.19)}$$

Appendix C. Translation and conversion of expansions for a biharmonic function

In this section the results of Gumerov and Duraiswami [39] are given for our definition of spherical harmonics. Let $\psi(\boldsymbol{x}) = \phi(\boldsymbol{x}) + x^2\omega(\boldsymbol{x})$ be a multipole or local expansion of a biharmonic function. We want to set the origin of the expansion at $\boldsymbol{t}$, *i.e.* we consider the new function (Fig. C1)

$$\begin{aligned}\hat{\psi}(\boldsymbol{x}) &= \psi(\boldsymbol{x}+\boldsymbol{t}) \\ &= \phi(\boldsymbol{x}+\boldsymbol{t}) + (\boldsymbol{x}+\boldsymbol{t})\cdot(\boldsymbol{x}+\boldsymbol{t})\omega(\boldsymbol{x}+\boldsymbol{t}) \\ &= \hat{\phi}(\boldsymbol{x}) + (x^2 + 2\boldsymbol{x}\cdot\boldsymbol{t} + t^2)\hat{\omega}(\boldsymbol{x}),\end{aligned} \tag{C.1}$$

where $\hat{\phi}$ and $\hat{\omega}$ are the same expansions as ϕ and ω, but with their origin at $\boldsymbol{t}$, *i.e.* their coefficients are deduced from the expansions ϕ and ω by translation or conversion operators of harmonic functions [24, 25]. We want to set Eq. (C.1) under the form

$$\hat{\psi}(\boldsymbol{x}) = \tilde{\phi}(\boldsymbol{x}) + x^2\tilde{\omega}(\boldsymbol{x}), \tag{C.2}$$

where $\tilde{\phi}$ and $\tilde{\omega}$ remain to be found. Operators which transform the coefficients of the expansion (ϕ, ω) into the coefficients of the expansion $(\tilde{\phi}, \tilde{\omega})$ are the translation/conversion operators which are used in the FMM.

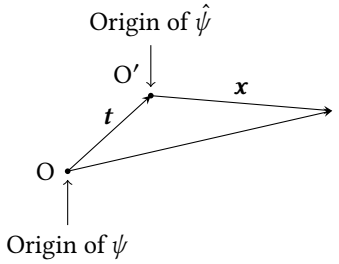

Figure C1. Change of center of expansion.

Two cases can be distinguished:

- For a multipole-to-multipole (M2M) transformation (translation), $\hat{\phi}(\boldsymbol{x})$ and $\hat{\omega}(\boldsymbol{x})$ are expanded with irregular solid harmonics. Eqs (B.14)–(B.16) can be used to write the term $2\boldsymbol{x}\cdot\boldsymbol{t}\hat{\omega}(\boldsymbol{x})$ as contributions to $\tilde{\phi}(\boldsymbol{x})$ and $\tilde{\omega}(\boldsymbol{x})$. We obtain

$$\tilde{\phi}_l^m = \hat{\phi}_l^m + t^2\hat{\omega}_l^m - \hat{\omega}_{l+1}^{m+1}\frac{t_1+it_2}{2l+3}s(m)C_{l+1}^{m+1} + \hat{\omega}_{l+1}^m\frac{2t_3}{2l+3}B_{l+1}^m + \hat{\omega}_{l+1}^{m-1}\frac{t_1-it_2}{2l+3}s(m-1)C_{l+1}^{-m+1} \tag{C.3}$$

$$\tilde{\omega}_l^m = \hat{\omega}_l^m + \hat{\omega}_{l-1}^{m+1}\frac{t_1+it_2}{2l-1}s(m)C_l^{-m} + \hat{\omega}_{l-1}^m\frac{2t_3}{2l-1}B_l^m - \hat{\omega}_{l-1}^{m-1}\frac{t_1-it_2}{2l-1}s(m-1)C_{l+1}^{m-1}. \tag{C.4}$$

These expressions correspond to expression 57 in Ref. [39] obtained with a different definition of spherical harmonics.

- For a multipole-to-local (M2L) or a local-to-local (L2L) transformation, $\hat{\phi}(\boldsymbol{x})$ and $\hat{\omega}(\boldsymbol{x})$ are expanded with regular solid harmonics. Eqs (B.17)–(B.19) can be used to write the term $2\boldsymbol{x}\cdot\boldsymbol{t}\hat{\omega}(\boldsymbol{x})$ as contributions to $\tilde{\phi}(\boldsymbol{x})$ and $\tilde{\omega}(\boldsymbol{x})$. We obtain

$$\tilde{\phi}_l^m = \hat{\phi}_l^m + t^2\hat{\omega}_l^m + \hat{\omega}_{l-1}^{m+1}\frac{t_1+it_2}{2l-1}s(m)C_l^{-m} + \hat{\omega}_{l-1}^m\frac{2t_3}{2l-1}B_l^m - \hat{\omega}_{l-1}^{m-1}\frac{t_1-it_2}{2l-1}s(m-1)C_{l+1}^{m-1} \tag{C.5}$$

$$\tilde{\omega}_l^m = \hat{\omega}_l^m - \hat{\omega}_{l+1}^{m+1}\frac{t_1+it_2}{2l+3}s(m)C_{l+1}^{m+1} + \hat{\omega}_{l+1}^m\frac{2t_3}{2l+3}B_{l+1}^m + \hat{\omega}_{l+1}^{m-1}\frac{t_1-it_2}{2l+3}s(m-1)C_{l+1}^{-m+1}. \tag{C.6}$$

  These expressions correspond to expression 56 in Ref. [39].

Appendix D. Derivatives of irregular solid harmonics

Derivatives of irregular solid harmonics are used in the local expansion of the strain field of a cavity (Eq. (25)) and a dislocation segment (Eqs (32)-(33)). They are also used to obtain the derivatives of regular solid harmonics (Appendix E). To determine them, it is convenient to use expression (B.6). The dependency of I_l^m functions on x, θ, φ is dropped for clarity.

First derivatives

- $m = 0$

$$\frac{\partial}{\partial x_1}(I_l^0) = \frac{1}{2}\sqrt{(l+1)(l+2)}(I_{l+1}^1 + I_{l+1}^{-1}) \tag{D.1}$$

$$\frac{\partial}{\partial x_2}(I_l^0) = -\frac{i}{2}\sqrt{(l+1)(l+2)}(I_{l+1}^1 - I_{l+1}^{-1}) \tag{D.2}$$

$$\frac{\partial}{\partial x_3}(I_l^0) = -(l+1)I_{l+1}^0 \tag{D.3}$$

- $m \geq 1$

$$\frac{\partial}{\partial x_1}(I_l^m) = \frac{1}{2}\left(\sqrt{(l+m+2)(l+m+1)}I_{l+1}^{m+1} - \sqrt{(l-m+2)(l-m+1)}I_{l+1}^{m-1}\right) \tag{D.4}$$

$$\frac{\partial}{\partial x_2}(I_l^m) = -\frac{i}{2}\left(\sqrt{(l+m+2)(l+m+1)}I_{l+1}^{m+1} + \sqrt{(l-m+2)(l-m+1)}I_{l+1}^{m-1}\right) \tag{D.5}$$

$$\frac{\partial}{\partial x_3}(I_l^m) = -\sqrt{(l+m+1)(l-m+1)}I_{l+1}^m \tag{D.6}$$

Second derivatives

- $m = 0$

$$\frac{\partial^2}{\partial x_1^2}(I_l^0) = \frac{1}{4}\sqrt{(l+1)(l+2)(l+3)(l+4)}I_{l+2}^2 - \frac{1}{2}(l+1)(l+2)I_{l+2}^0 + \frac{1}{4}\sqrt{(l+1)(l+2)(l+3)(l+4)}I_{l+2}^{-2} \tag{D.7}$$

$$\frac{\partial^2}{\partial x_2^2}(I_l^0) = -\frac{1}{4}\sqrt{(l+1)(l+2)(l+3)(l+4)}I_{l+2}^2 - \frac{1}{2}(l+1)(l+2)I_{l+2}^0 - \frac{1}{4}\sqrt{(l+1)(l+2)(l+3)(l+4)}I_{l+2}^{-2} \quad \text{(D.8)}$$

$$\frac{\partial^2}{\partial x_3^2}(I_l^0) = (l+1)(l+2)I_{l+2}^0 \quad \text{(D.9)}$$

$$\frac{\partial^2}{\partial x_1 \partial x_2}(I_l^0) = -\frac{i}{4}\sqrt{(l+1)(l+2)(l+3)(l+4)}I_{l+2}^2 + \frac{i}{4}\sqrt{(l+1)(l+2)(l+3)(l+4)}I_{l+2}^{-2} \quad \text{(D.10)}$$

$$\frac{\partial^2}{\partial x_2 \partial x_3}(I_l^0) = \frac{i}{2}(l+1)\sqrt{(l+2)(l+3)}(I_{l+2}^1 - I_{l+2}^{-1}) \quad \text{(D.11)}$$

$$\frac{\partial^2}{\partial x_1 \partial x_3}(I_l^0) = -\frac{1}{2}(l+1)\sqrt{(l+2)(l+3)}(I_{l+2}^1 + I_{l+2}^{-1}) \quad \text{(D.12)}$$

- $m = 1$

$$\frac{\partial^2}{\partial x_1^2}(I_l^1) = \frac{1}{4}\sqrt{(l+2)(l+3)(l+4)(l+5)}I_{l+2}^3 - \frac{1}{2}\sqrt{l(l+1)(l+2)(l+3)}I_{l+2}^1 - \frac{1}{4}\sqrt{l(l+1)(l+2)(l+3)}I_{l+2}^{-1} \quad \text{(D.13)}$$

$$\frac{\partial^2}{\partial x_2^2}(I_l^1) = -\frac{1}{4}\sqrt{(l+2)(l+3)(l+4)(l+5)}I_{l+2}^3 - \frac{1}{2}\sqrt{l(l+1)(l+2)(l+3)}I_{l+2}^1 + \frac{1}{4}\sqrt{l(l+1)(l+2)(l+3)}I_{l+2}^{-1} \quad \text{(D.14)}$$

$$\frac{\partial^2}{\partial x_3^2}(I_l^1) = \sqrt{l(l+1)(l+2)(l+3)}I_{l+2}^1 \quad \text{(D.15)}$$

$$\frac{\partial^2}{\partial x_1 \partial x_2}(I_l^1) = -\frac{i}{4}\sqrt{(l+2)(l+3)(l+4)(l+5)}I_{l+2}^3 - \frac{i}{4}\sqrt{l(l+1)(l+2)(l+3)}I_{l+2}^{-1} \quad \text{(D.16)}$$

$$\frac{\partial^2}{\partial x_2 \partial x_3}(I_l^1) = \frac{i}{2}\sqrt{l(l+2)(l+3)(l+4)}I_{l+2}^2 + \frac{i}{2}(l+2)\sqrt{l(l+1)}I_{l+2}^0 \quad \text{(D.17)}$$

$$\frac{\partial^2}{\partial x_1 \partial x_3}(I_l^1) = -\frac{1}{2}\sqrt{l(l+2)(l+3)(l+4)}I_{l+2}^2 + \frac{1}{2}(l+2)\sqrt{l(l+1)}I_{l+2}^0 \quad \text{(D.18)}$$

- $m \geq 2$

$$\frac{\partial^2}{\partial x_1^2}(I_l^m) = \frac{1}{4}\sqrt{(l+m+1)(l+m+2)(l+m+3)(l+m+4)}I_{l+2}^{m+2} - \frac{1}{2}\sqrt{(l-m+2)(l-m+1)(l+m+1)(l+m+2)}I_{l+2}^{m} + \frac{1}{4}\sqrt{(l-m+1)(l-m+2)(l-m+3)(l-m+4)}I_{l+2}^{m-2} \quad \text{(D.19)}$$

$$\frac{\partial^2}{\partial x_2^2}(I_l^m) = -\frac{1}{4}\sqrt{(l+m+1)(l+m+2)(l+m+3)(l+m+4)}I_{l+2}^{m+2} - \frac{1}{2}\sqrt{(l-m+1)(l-m+2)(l+m+1)(l+m+2)}I_{l+2}^{m} - \frac{1}{4}\sqrt{(l-m+1)(l-m+2)(l-m+3)(l-m+4)}I_{l+2}^{m-2} \quad \text{(D.20)}$$

$$\frac{\partial^2}{\partial x_3^2}(I_l^m) = \sqrt{(l-m+1)(l-m+2)(l+m+1)(l+m+2)}I_{l+2}^{m} \quad \text{(D.21)}$$

$$\frac{\partial^2}{\partial x_1 \partial x_2}(I_l^m) = -\frac{i}{4}\sqrt{(l+m+1)(l+m+2)(l+m+3)(l+m+4)}I_{l+2}^{m+2} + \frac{i}{4}\sqrt{(l-m+1)(l-m+2)(l-m+3)(l-m+4)}I_{l+2}^{m-2} \quad \text{(D.22)}$$

$$\frac{\partial^2}{\partial x_2 \partial x_3}(I_l^m) = \frac{i}{2}\sqrt{(l-m+1)(l+m+1)(l+m+2)(l+m+3)}I_{l+2}^{m+1} + \frac{i}{2}\sqrt{(l-m+1)(l-m+2)(l-m+3)(l+m+1)}I_{l+2}^{m-1} \quad \text{(D.23)}$$

$$\frac{\partial^2}{\partial x_1 \partial x_3}(I_l^m) = -\frac{1}{2}\sqrt{(l-m+1)(l+m+1)(l+m+2)(l+m+3)}I_{l+2}^{m+1} + \frac{1}{2}\sqrt{(l-m+1)(l-m+2)(l-m+3)(l+m+1)}I_{l+2}^{m-1} \quad \text{(D.24)}$$

675 *Third derivatives*

- $m = 0$

$$\frac{\partial^3}{\partial x_1^3}(I_l^0) = \frac{1}{8}\sqrt{(l+1)(l+2)(l+3)(l+4)(l+5)(l+6)}(I_{l+3}^3 + I_{l+3}^{-3}) - \frac{3}{8}(l+1)(l+2)\sqrt{(l+3)(l+4)}(I_{l+3}^1 + I_{l+3}^{-1}) \quad \text{(D.25)}$$

$$\frac{\partial^3}{\partial x_2^3}(I_l^0) = \frac{i}{8}\sqrt{(l+1)(l+2)(l+3)(l+4)(l+5)(l+6)}(I_{l+3}^3 - I_{l+3}^{-3}) + \frac{3i}{8}(l+1)(l+2)\sqrt{(l+3)(l+4)}(I_{l+3}^1 - I_{l+3}^{-1}) \quad \text{(D.26)}$$

$$\frac{\partial^3}{\partial x_3^3}(I_l^0) = -(l+1)(l+2)(l+3)I_{l+3}^0 \tag{D.27}$$

$$\frac{\partial^3}{\partial x_1^2 \partial x_2}(I_l^0) = -\frac{i}{8}\sqrt{(l+1)(l+2)(l+3)(l+4)(l+5)(l+6)}(I_{l+3}^3 - I_{l+3}^{-3}) + \frac{i}{8}(l+1)(l+2)\sqrt{(l+3)(l+4)}(I_{l+3}^1 - I_{l+3}^{-1}) \tag{D.28}$$

$$\frac{\partial^3}{\partial x_1^2 \partial x_3}(I_l^0) = -\frac{1}{4}(l+1)\sqrt{(l+2)(l+3)(l+4)(l+5)}(I_{l+3}^2 + I_{l+3}^{-2}) + \frac{1}{2}(l+1)(l+2)(l+3)I_{l+3}^0 \tag{D.29}$$

$$\frac{\partial^3}{\partial x_1 \partial x_2^2}(I_l^0) = -\frac{1}{8}\sqrt{(l+1)(l+2)(l+3)(l+4)(l+5)(l+6)}(I_{l+3}^3 + I_{l+3}^{-3}) - \frac{1}{8}(l+1)(l+2)\sqrt{(l+3)(l+4)}(I_{l+3}^1 + I_{l+3}^{-1}) \tag{D.30}$$

$$\frac{\partial^3}{\partial x_2^2 \partial x_3}(I_l^0) = \frac{1}{4}(l+1)\sqrt{(l+2)(l+3)(l+4)(l+5)}(I_{l+3}^2 + I_{l+3}^{-2}) + \frac{1}{2}(l+1)(l+2)(l+3)I_{l+3}^0 \tag{D.31}$$

$$\frac{\partial^3}{\partial x_1 \partial x_3^2}(I_l^0) = \frac{1}{2}(l+1)(l+2)\sqrt{(l+3)(l+4)}(I_{l+3}^1 + I_{l+3}^{-1}) \tag{D.32}$$

$$\frac{\partial^3}{\partial x_2 \partial x_3^2}(I_l^0) = -\frac{i}{2}(l+1)(l+2)\sqrt{(l+3)(l+4)}(I_{l+3}^1 - I_{l+3}^{-1}) \tag{D.33}$$

$$\frac{\partial^3}{\partial x_1 \partial x_2 \partial x_3}(I_l^0) = \frac{i}{4}(l+1)\sqrt{(l+2)(l+3)(l+4)(l+5)}(I_{l+3}^2 - I_{l+3}^{-2}) \tag{D.34}$$

- $m = 1$

$$\frac{\partial^3}{\partial x_1^3}(I_l^1) = \frac{1}{8}\sqrt{(l+2)(l+3)(l+4)(l+5)(l+6)(l+7)}I_{l+3}^4 - \frac{3}{8}\sqrt{l(l+1)(l+2)(l+3)(l+4)(l+5)}I_{l+3}^2 + \frac{3}{8}(l+2)(l+3)\sqrt{l(l+1)}I_{l+3}^0 - \frac{1}{8}\sqrt{l(l+1)(l+2)(l+3)(l+4)(l+5)}I_{l+3}^{-2} \tag{D.35}$$

$$\frac{\partial^3}{\partial x_2^3}(I_l^1) = \frac{i}{8}\sqrt{(l+2)(l+3)(l+4)(l+5)(l+6)(l+7)}I_{l+3}^4 + \frac{3i}{8}\sqrt{l(l+1)(l+2)(l+3)(l+4)(l+5)}I_{l+3}^2 + \frac{3i}{8}(l+2)(l+3)\sqrt{l(l+1)}I_{l+3}^0 + \frac{i}{8}\sqrt{l(l+1)(l+2)(l+3)(l+4)(l+5)}I_{l+3}^{-2} \quad \text{(D.36)}$$

$$\frac{\partial^3}{\partial x_3^3}(I_l^1) = -(l+2)\sqrt{l(l+1)(l+3)(l+4)}I_{l+3}^1 \quad \text{(D.37)}$$

$$\frac{\partial^3}{\partial x_1^2 \partial x_2}(I_l^1) = -\frac{i}{8}\sqrt{(l+2)(l+3)(l+4)(l+5)(l+6)(l+7)}I_{l+3}^4 + \frac{i}{8}\sqrt{l(l+1)(l+2)(l+3)(l+4)(l+5)}I_{l+3}^2 + \frac{i}{8}(l+2)(l+3)\sqrt{l(l+1)}I_{l+3}^0 - \frac{i}{8}\sqrt{l(l+1)(l+2)(l+3)(l+4)(l+5)}I_{l+3}^{-2} \quad \text{(D.38)}$$

$$\frac{\partial^3}{\partial x_1^2 \partial x_3}(I_l^1) = -\frac{1}{4}\sqrt{l(l+2)(l+3)(l+4)(l+5)(l+6)}I_{l+3}^3 + \frac{1}{2}(l+2)\sqrt{l(l+1)(l+3)(l+4)}I_{l+3}^1 + \frac{1}{4}(l+2)\sqrt{l(l+1)(l+3)(l+4)}I_{l+3}^{-1} \quad \text{(D.39)}$$

$$\frac{\partial^3}{\partial x_1 \partial x_2^2}(I_l^1) = -\frac{1}{8}\sqrt{(l+2)(l+3)(l+4)(l+5)(l+6)(l+7)}I_{l+3}^4 - \frac{1}{8}\sqrt{l(l+1)(l+2)(l+3)(l+4)(l+5)}I_{l+3}^2 + \frac{1}{8}(l+2)(l+3)\sqrt{l(l+1)}I_{l+3}^0 + \frac{1}{8}\sqrt{l(l+1)(l+2)(l+3)(l+4)(l+5)}I_{l+3}^{-2} \quad \text{(D.40)}$$

$$\frac{\partial^3}{\partial x_2^2 \partial x_3}(I_l^1) = \frac{1}{4}\sqrt{l(l+2)(l+3)(l+4)(l+5)(l+6)}I_{l+3}^3 + \frac{1}{2}(l+2)\sqrt{l(l+1)(l+3)(l+4)}I_{l+3}^1 - \frac{1}{4}(l+2)\sqrt{l(l+1)(l+3)(l+4)}I_{l+3}^{-1} \quad \text{(D.41)}$$

$$\frac{\partial^3}{\partial x_1 \partial x_3^2}(I_l^1) = \frac{1}{2}\sqrt{l(l+1)(l+2)(l+3)(l+4)(l+5)}I_{l+3}^2 - \frac{1}{2}(l+2)(l+3)\sqrt{l(l+1)}I_{l+3}^0 \quad \text{(D.42)}$$

$$\frac{\partial^3}{\partial x_2 \partial x_3^2}(I_l^1) = -\frac{i}{2}\sqrt{l(l+1)(l+2)(l+3)(l+4)(l+5)}I_{l+3}^2 - \frac{i}{2}(l+2)(l+3)\sqrt{l(l+1)}I_{l+3}^0 \quad \text{(D.43)}$$

$$\frac{\partial^3}{\partial x_1 \partial x_2 \partial x_3}(I_l^1) = \frac{i}{4}\sqrt{l(l+2)(l+3)(l+4)(l+5)(l+6)}I_{l+3}^3 + \frac{i}{4}(l+2)\sqrt{l(l+1)(l+3)(l+4)}I_{l+3}^{-1} \quad \text{(D.44)}$$

- $m = 2$

$$\frac{\partial^3}{\partial x_1^3}(I_l^2) = \frac{1}{8}\sqrt{(l+3)(l+4)(l+5)(l+6)(l+7)(l+8)}I_{l+3}^5 - \frac{3}{8}\sqrt{(l-1)l(l+3)(l+4)(l+5)(l+6)}I_{l+3}^3 + \frac{3}{8}\sqrt{(l-1)l(l+1)(l+2)(l+3)(l+4)}I_{l+3}^1 + \frac{1}{8}\sqrt{(l-1)l(l+1)(l+2)(l+3)(l+4)}I_{l+3}^{-1} \quad \text{(D.45)}$$

$$\frac{\partial^3}{\partial x_2^3}(I_l^2) = \frac{i}{8}\sqrt{(l+3)(l+4)(l+5)(l+6)(l+7)(l+8)}I_{l+3}^5 + \frac{3i}{8}\sqrt{(l-1)l(l+3)(l+4)(l+5)(l+6)}I_{l+3}^3 + \frac{3i}{8}\sqrt{(l-1)l(l+1)(l+2)(l+3)(l+4)}I_{l+3}^1 - \frac{i}{8}\sqrt{(l-1)l(l+1)(l+2)(l+3)(l+4)}I_{l+3}^{-1} \quad \text{(D.46)}$$

$$\frac{\partial^3}{\partial x_3^3}(I_l^2) = -\sqrt{(l-1)l(l+1)(l+3)(l+4)(l+5)}I_{l+3}^2 \quad \text{(D.47)}$$

$$\frac{\partial^3}{\partial x_1^2 \partial x_2}(I_l^2) = -\frac{i}{8}\sqrt{(l+3)(l+4)(l+5)(l+6)(l+7)(l+8)}I_{l+3}^5 + \frac{i}{8}\sqrt{(l-1)l(l+3)(l+4)(l+5)(l+6)}I_{l+3}^3 + \frac{i}{8}\sqrt{(l-1)l(l+1)(l+2)(l+3)(l+4)}I_{l+3}^1 + \frac{i}{8}\sqrt{(l-1)l(l+1)(l+2)(l+3)(l+4)}I_{l+3}^{-1} \quad \text{(D.48)}$$

$$\frac{\partial^3}{\partial x_1^2 \partial x_3}(I_l^2) = -\frac{1}{4}\sqrt{(l-1)(l+3)(l+4)(l+5)(l+6)(l+7)}I_{l+3}^4 + \frac{1}{2}\sqrt{(l-1)l(l+1)(l+3)(l+4)(l+5)}I_{l+3}^2 - \frac{1}{4}(l+3)\sqrt{(l-1)l(l+1)(l+2)}I_{l+3}^0 \quad \text{(D.49)}$$

$$\frac{\partial^3}{\partial x_1 \partial x_2^2}(I_l^2) = -\frac{1}{8}\sqrt{(l+3)(l+4)(l+5)(l+6)(l+7)(l+8)}I_{l+3}^5 - \frac{1}{8}\sqrt{(l-1)l(l+3)(l+4)(l+5)(l+6)}I_{l+3}^3 + \frac{1}{8}\sqrt{(l-1)l(l+1)(l+2)(l+3)(l+4)}I_{l+3}^1 - \frac{1}{8}\sqrt{(l-1)l(l+1)(l+2)(l+3)(l+4)}I_{l+3}^{-1} \quad \text{(D.50)}$$

$$\frac{\partial^3}{\partial x_2^2 \partial x_3}(I_l^2) = \frac{1}{4}\sqrt{(l-1)(l+3)(l+4)(l+5)(l+6)(l+7)}I_{l+3}^4 + \frac{1}{2}\sqrt{(l-1)l(l+1)(l+3)(l+4)(l+5)}I_{l+3}^2 + \frac{1}{4}(l+3)\sqrt{(l-1)l(l+1)(l+2)}I_{l+3}^0 \quad \text{(D.51)}$$

$$\frac{\partial^3}{\partial x_1 \partial x_3^2}(I_l^2) = \frac{1}{2}\sqrt{(l-1)l(l+3)(l+4)(l+5)(l+6)}I_{l+3}^3 - \frac{1}{2}\sqrt{(l-1)l(l+1)(l+2)(l+3)(l+4)}I_{l+3}^1 \quad \text{(D.52)}$$

$$\frac{\partial^3}{\partial x_2 \partial x_3^2}(I_l^2) = -\frac{i}{2}\sqrt{(l-1)l(l+3)(l+4)(l+5)(l+6)}I_{l+3}^3 - \frac{i}{2}\sqrt{(l-1)l(l+1)(l+2)(l+3)(l+4)}I_{l+3}^1 \quad \text{(D.53)}$$

$$\frac{\partial^3}{\partial x_1 \partial x_2 \partial x_3}(I_l^2) = \frac{i}{4}\sqrt{(l-1)(l+3)(l+4)(l+5)(l+6)(l+7)}I_{l+3}^4 - \frac{i}{4}(l+3)\sqrt{(l-1)l(l+1)(l+2)}I_{l+3}^0 \quad \text{(D.54)}$$

- $m \geq 3$

$$\frac{\partial^3}{\partial x_1^3}(I_l^m) = \frac{1}{8}\sqrt{(l+m+1)(l+m+2)(l+m+3)(l+m+4)(l+m+5)(l+m+6)}I_{l+3}^{m+3}$$
$$-\frac{3}{8}\sqrt{(l-m+1)(l-m+2)(l+m+1)(l+m+2)(l+m+3)(l+m+4)}I_{l+3}^{m+1}$$
$$+\frac{3}{8}\sqrt{(l-m+1)(l-m+2)(l-m+3)(l-m+4)(l+m+1)(l+m+2)}I_{l+3}^{m-1}$$
$$-\frac{1}{8}\sqrt{(l-m+1)(l-m+2)(l-m+3)(l-m+4)(l-m+5)(l-m+6)}I_{l+3}^{m-3} \tag{D.55}$$

$$\frac{\partial^3}{\partial x_2^3}(I_l^m) = \frac{i}{8}\sqrt{(l+m+1)(l+m+2)(l+m+3)(l+m+4)(l+m+5)(l+m+6)}I_{l+3}^{m+3}$$
$$+\frac{3i}{8}\sqrt{(l-m+1)(l-m+2)(l+m+1)(l+m+2)(l+m+3)(l+m+4)}I_{l+3}^{m+1}$$
$$+\frac{3i}{8}\sqrt{(l-m+1)(l-m+2)(l-m+3)(l-m+4)(l+m+1)(l+m+2)}I_{l+3}^{m-1}$$
$$+\frac{i}{8}\sqrt{(l-m+1)(l-m+2)(l-m+3)(l-m+4)(l-m+5)(l-m+6)}I_{l+3}^{m-3} \tag{D.56}$$

$$\frac{\partial^3}{\partial x_3^3}(I_l^m) = -\sqrt{(l-m+1)(l-m+2)(l-m+3)(l+m+1)(l+m+2)(l+m+3)}I_{l+3}^{m} \tag{D.57}$$

$$\frac{\partial^3}{\partial x_1^2 \partial x_2}(I_l^m) = -\frac{i}{8}\sqrt{(l+m+1)(l+m+2)(l+m+3)(l+m+4)(l+m+5)(l+m+6)}I_{l+3}^{m+3}$$
$$+\frac{i}{8}\sqrt{(l-m+1)(l-m+2)(l+m+1)(l+m+2)(l+m+3)(l+m+4)}I_{l+3}^{m+1}$$
$$+\frac{i}{8}\sqrt{(l-m+1)(l-m+2)(l-m+3)(l-m+4)(l+m+1)(l+m+2)}I_{l+3}^{m-1}$$
$$-\frac{i}{8}\sqrt{(l-m+1)(l-m+2)(l-m+3)(l-m+4)(l-m+5)(l-m+6)}I_{l+3}^{m-3} \tag{D.58}$$

$$\frac{\partial^3}{\partial x_1^2 \partial x_3}(I_l^m) = -\frac{1}{4}\sqrt{(l-m+1)(l+m+1)(l+m+2)(l+m+3)(l+m+4)(l+m+5)}I_{l+3}^{m+2}$$
$$+\frac{1}{2}\sqrt{(l-m+1)(l-m+2)(l-m+3)(l+m+1)(l+m+2)(l+m+3)}I_{l+3}^{m}$$
$$-\frac{1}{4}\sqrt{(l-m+1)(l-m+2)(l-m+3)(l-m+4)(l-m+5)(l+m+1)}I_{l+3}^{m-2} \tag{D.59}$$

$$\frac{\partial^3}{\partial x_1 \partial x_2^2}(I_l^m) = -\frac{1}{8}\sqrt{(l+m+1)(l+m+2)(l+m+3)(l+m+4)(l+m+5)(l+m+6)}I_{l+3}^{m+3}$$
$$-\frac{1}{8}\sqrt{(l-m+1)(l-m+2)(l+m+1)(l+m+2)(l+m+3)(l+m+4)}I_{l+3}^{m+1}$$
$$+\frac{1}{8}\sqrt{(l-m+1)(l-m+2)(l-m+3)(l-m+4)(l+m+1)(l+m+2)}I_{l+3}^{m-1}$$
$$+\frac{1}{8}\sqrt{(l-m+1)(l-m+2)(l-m+3)(l-m+4)(l-m+5)(l-m+6)}I_{l+3}^{m-3} \tag{D.60}$$

$$\frac{\partial^3}{\partial x_2^2 \partial x_3}(I_l^m) = \frac{1}{4}\sqrt{(l-m+1)(l+m+1)(l+m+2)(l+m+3)(l+m+4)(l+m+5)}I_{l+3}^{m+2}$$
$$+\frac{1}{2}\sqrt{(l-m+1)(l-m+2)(l-m+3)(l+m+1)(l+m+2)(l+m+3)}I_{l+3}^{m}$$
$$+\frac{1}{4}\sqrt{(l-m+1)(l-m+2)(l-m+3)(l-m+4)(l-m+5)(l+m+1)}I_{l+3}^{m-2} \tag{D.61}$$

$$\frac{\partial^3}{\partial x_1 \partial x_3^2}(I_l^m) = \frac{1}{2}\sqrt{(l-m+1)(l-m+2)(l+m+1)(l+m+2)(l+m+3)(l+m+4)}I_{l+3}^{m+1}$$
$$-\frac{1}{2}\sqrt{(l-m+1)(l-m+2)(l-m+3)(l-m+4)(l+m+1)(l+m+2)}I_{l+3}^{m-1} \tag{D.62}$$

$$\frac{\partial^3}{\partial x_2 \partial x_3^2}(I_l^m) = -\frac{i}{2}\sqrt{(l-m+1)(l-m+2)(l+m+1)(l+m+2)(l+m+3)(l+m+4)}I_{l+3}^{m+1}$$
$$-\frac{i}{2}\sqrt{(l-m+1)(l-m+2)(l-m+3)(l-m+4)(l+m+1)(l+m+2)}I_{l+3}^{m-1} \tag{D.63}$$

$$\frac{\partial^3}{\partial x_1 \partial x_2 \partial x_3}(I_l^m) = \frac{i}{4}\sqrt{(l-m+1)(l+m+1)(l+m+2)(l+m+3)(l+m+4)(l+m+5)}I_{l+3}^{m+2}$$
$$-\frac{i}{4}\sqrt{(l-m+1)(l-m+2)(l-m+3)(l-m+4)(l-m+5)(l+m+1)}I_{l+3}^{m-2} \tag{D.64}$$

Appendix E. Derivatives of regular solid harmonics

Derivatives of regular solid harmonics are useful for the multipole expansion of the strain field of a cavity (Eq. (23)) and a dislocation segment (Eqs. (28)-(29)). They can be obtained by writing $R_l^m(x,\theta,\varphi) = x^{2l+1}I_l^m(x,\theta,\varphi)$, then using Eq. (B.6) and recursion formulas (B.12) and (B.13). First and second derivatives are given in Ref. [27]. They are recalled here for the sake of completeness.

First derivatives

- $m = 0$

$$\frac{\partial}{\partial x_1}(R_l^0) = \frac{1}{2}\sqrt{l(l-1)}\left(R_{l-1}^{-1} + R_{l-1}^{1}\right) \tag{E.1}$$

$$\frac{\partial}{\partial x_2}(R_l^0) = -\frac{i}{2}\sqrt{l(l-1)}\left(R_{l-1}^{1} - R_{l-1}^{-1}\right) \tag{E.2}$$

$$\frac{\partial}{\partial x_3}(R_l^0) = lR_{l-1}^0 \tag{E.3}$$

- $m \geq 1$

$$\frac{\partial}{\partial x_1}(R_l^m) = \frac{1}{2}\left(\sqrt{(l-m)(l-m-1)}R_{l-1}^{m+1} - \sqrt{(l+m)(l+m-1)}R_{l-1}^{m-1}\right) \tag{E.4}$$

$$\frac{\partial}{\partial x_2}(R_l^m) = -\frac{i}{2}\left(\sqrt{(l-m)(l-m-1)}R_{l-1}^{m+1} + \sqrt{(l+m)(l+m-1)}R_{l-1}^{m-1}\right) \tag{E.5}$$

$$\frac{\partial}{\partial x_3}(R_l^m) = \sqrt{(l+m)(l-m)}R_{l-1}^m \tag{E.6}$$

Second derivatives

- $m = 0$

$$\frac{\partial^2}{\partial x_1^2}(R_l^0) = \frac{1}{4}\sqrt{l(l-1)(l-2)(l-3)}\left(R_{l-2}^{2} + R_{l-2}^{-2}\right) - \frac{1}{2}l(l-1)R_{l-2}^0 \tag{E.7}$$

$$\frac{\partial^2}{\partial x_2^2}(R_l^0) = -\frac{1}{4}\sqrt{l(l-1)(l-2)(l-3)}\left(R_{l-2}^{2} + R_{l-2}^{-2}\right) - \frac{1}{2}l(l-1)R_{l-2}^0 \tag{E.8}$$

$$\frac{\partial^2}{\partial x_3^2}(R_l^0) = l(l-1)R_{l-2}^0 \tag{E.9}$$

$$\frac{\partial^2}{\partial x_1 \partial x_2}(R_l^0) = -\frac{i}{4}\sqrt{l(l-1)(l-2)(l-3)}\left(R_{l-2}^{2} - R_{l-2}^{-2}\right) \tag{E.10}$$

$$\frac{\partial^2}{\partial x_2 \partial x_3}(R_l^0) = -\frac{i}{2}l\sqrt{(l-1)(l-2)}\left(R_{l-2}^{1} - R_{l-2}^{-1}\right) \tag{E.11}$$

$$\frac{\partial^2}{\partial x_1 \partial x_3}(R_l^0) = \frac{1}{2}l\sqrt{(l-1)(l-2)}\left(R_{l-2}^{1} + R_{l-2}^{-1}\right) \tag{E.12}$$

- $m = 1$

$$\frac{\partial^2}{\partial x_1^2}(R_l^1) = \frac{1}{4}\sqrt{(l-1)(l-2)(l-3)(l-4)}R_{l-2}^3 - \frac{1}{2}\sqrt{(l+1)l(l-1)(l-2)}R_{l-2}^1 - \frac{1}{4}\sqrt{(l+1)l(l-1)(l-2)}R_{l-2}^{-1} \tag{E.13}$$

$$\frac{\partial^2}{\partial x_2^2}(R_l^1) = -\frac{1}{4}\sqrt{(l-1)(l-2)(l-3)(l-4)}R_{l-2}^3 - \frac{1}{2}\sqrt{(l+1)l(l-1)(l-2)}R_{l-2}^1 + \frac{1}{4}\sqrt{(l+1)l(l-1)(l-2)}R_{l-2}^{-1} \tag{E.14}$$

$$\frac{\partial^2}{\partial x_3^2}(R_l^1) = \sqrt{(l+1)l(l-1)(l-2)}R_{l-2}^1 \tag{E.15}$$

$$\frac{\partial^2}{\partial x_1 \partial x_2}(R_l^1) = -\frac{i}{4}\sqrt{(l-1)(l-2)(l-3)(l-4)}R_{l-2}^3 - \frac{i}{4}\sqrt{(l+1)l(l-1)(l-2)}R_{l-2}^{-1} \tag{E.16}$$

$$\frac{\partial^2}{\partial x_2 \partial x_3}(R_l^1) = -\frac{i}{2}\sqrt{(l+1)(l-1)(l-2)(l-3)}R_{l-2}^2 - \frac{i}{2}\sqrt{(l+1)l(l-1)^2}R_{l-2}^0 \tag{E.17}$$

$$\frac{\partial^2}{\partial x_1 \partial x_3}(R_l^1) = \frac{1}{2}\sqrt{(l+1)(l-1)(l-2)(l-3)}R_{l-2}^2 - \frac{1}{2}\sqrt{(l+1)l(l-1)^2}R_{l-2}^0 \tag{E.18}$$

- $m \geq 2$

$$\begin{aligned}\frac{\partial^2}{\partial x_1^2}(R_l^m) = {} & \frac{1}{4}\sqrt{(l-m)(l-m-1)(l-m-2)(l-m-3)}R_{l-2}^{m+2} \\ & - \frac{1}{2}\sqrt{(l+m)(l+m-1)(l-m)(l-m-1)}R_{l-2}^m \\ & + \frac{1}{4}\sqrt{(l+m)(l+m-1)(l+m-2)(l+m-3)}R_{l-2}^{m-2}\end{aligned} \tag{E.19}$$

$$\begin{aligned}\frac{\partial^2}{\partial x_2^2}(R_l^m) = {} & -\frac{1}{4}\sqrt{(l-m)(l-m-1)(l-m-2)(l-m-3)}R_{l-2}^{m+2} \\ & - \frac{1}{2}\sqrt{(l+m)(l+m-1)(l-m)(l-m-1)}R_{l-2}^m \\ & - \frac{1}{4}\sqrt{(l+m)(l+m-1)(l+m-2)(l+m-3)}R_{l-2}^{m-2}\end{aligned} \tag{E.20}$$

$$\frac{\partial^2}{\partial x_3^2}(R_l^m) = \sqrt{(l+m)(l+m-1)(l-m)(l-m-1)}R_{l-2}^m \tag{E.21}$$

$$\begin{aligned}\frac{\partial^2}{\partial x_1 \partial x_2}(R_l^m) = {} & -\frac{i}{4}\sqrt{(l-m)(l-m-1)(l-m-2)(l-m-3)}R_{l-2}^{m+2} \\ & + \frac{i}{4}\sqrt{(l+m)(l+m-1)(l+m-2)(l+m-3)}R_{l-2}^{m-2}\end{aligned} \tag{E.22}$$

$$\begin{aligned}\frac{\partial^2}{\partial x_2 \partial x_3}(R_l^m) = {} & -\frac{i}{2}\sqrt{(l+m)(l-m)(l-m-1)(l-m-2)}R_{l-2}^{m+1} \\ & - \frac{i}{2}\sqrt{(l+m)(l+m-1)(l+m-2)(l-m)}R_{l-2}^{m-1}\end{aligned} \tag{E.23}$$

$$\begin{aligned}\frac{\partial^2}{\partial x_1 \partial x_3}(R_l^m) = {} & \frac{1}{2}\sqrt{(l+m)(l-m)(l-m-1)(l-m-2)}R_{l-2}^{m+1} \\ & - \frac{1}{2}\sqrt{(l+m)(l+m-1)(l+m-2)(l-m)}R_{l-2}^{m-1}\end{aligned} \tag{E.24}$$

Third derivatives

- $m = 0$

$$\frac{\partial^3}{\partial x_1^3}(R_l^0) = \frac{1}{8}\sqrt{l(l-1)(l-2)(l-3)(l-4)(l-5)}\left(R_{l-3}^3 + R_{l-3}^{-3}\right) - \frac{3}{8}l(l-1)\sqrt{(l-2)(l-3)}\left(R_{l-3}^1 + R_{l-3}^{-1}\right) \quad \text{(E.25)}$$

$$\frac{\partial^3}{\partial x_2^3}(R_l^0) = \frac{i}{8}\sqrt{l(l-1)(l-2)(l-3)(l-4)(l-5)}\left(R_{l-3}^3 - R_{l-3}^{-3}\right) + \frac{3i}{8}l(l-1)\sqrt{(l-2)(l-3)}\left(R_{l-3}^1 - R_{l-3}^{-1}\right) \quad \text{(E.26)}$$

$$\frac{\partial^3}{\partial x_3^3}(R_l^0) = l(l-1)(l-2)R_{l-3}^0 \quad \text{(E.27)}$$

$$\frac{\partial^3}{\partial x_1^2 \partial x_2}(R_l^0) = -\frac{i}{8}\sqrt{l(l-1)(l-2)(l-3)(l-4)(l-5)}\left(R_{l-3}^3 - R_{l-3}^{-3}\right) + \frac{i}{8}l(l-1)\sqrt{(l-2)(l-3)}\left(R_{l-3}^1 - R_{l-3}^{-1}\right) \quad \text{(E.28)}$$

$$\frac{\partial^3}{\partial x_1^2 \partial x_3}(R_l^0) = \frac{1}{4}\sqrt{l^2(l-1)(l-2)(l-3)(l-4)}\left(R_{l-3}^2 + R_{l-3}^{-2}\right) - \frac{1}{2}l(l-1)(l-2)R_{l-3}^0 \quad \text{(E.29)}$$

$$\frac{\partial^3}{\partial x_1 \partial x_2^2}(R_l^0) = -\frac{1}{8}\sqrt{l(l-1)(l-2)(l-3)(l-4)(l-5)}\left(R_{l-3}^3 + R_{l-3}^{-3}\right) - \frac{1}{8}l(l-1)\sqrt{(l-2)(l-3)}\left(R_{l-3}^1 + R_{l-3}^{-1}\right) \quad \text{(E.30)}$$

$$\frac{\partial^3}{\partial x_2^2 \partial x_3}(R_l^0) = -\frac{1}{4}\sqrt{l^2(l-1)(l-2)(l-3)(l-4)}\left(R_{l-3}^2 + R_{l-3}^{-2}\right) - \frac{1}{2}l(l-1)(l-2)R_{l-3}^0 \quad \text{(E.31)}$$

$$\frac{\partial^3}{\partial x_1 \partial x_3^2}(R_l^0) = \frac{1}{2}l(l-1)\sqrt{(l-2)(l-3)}\left(R_{l-3}^1 + R_{l-3}^{-1}\right) \quad \text{(E.32)}$$

$$\frac{\partial^3}{\partial x_2 \partial x_3^2}(R_l^0) = -\frac{i}{2}l(l-1)\sqrt{(l-2)(l-3)}\left(R_{l-3}^1 - R_{l-3}^{-1}\right) \quad \text{(E.33)}$$

$$\frac{\partial^3}{\partial x_1 \partial x_2 \partial x_3}(R_l^0) = -\frac{i}{4}\sqrt{l^2(l-1)(l-2)(l-3)(l-4)}\left(R_{l-3}^2 - R_{l-3}^{-2}\right) \quad \text{(E.34)}$$

- $m = 1$

$$\frac{\partial^3}{\partial x_1^3}(R_l^1) = \frac{1}{8}\sqrt{(l-1)(l-2)(l-3)(l-4)(l-5)(l-6)}R_{l-3}^4 - \frac{3}{8}\sqrt{(l+1)l(l-1)(l-2)(l-3)(l-4)}R_{l-3}^2 + \frac{3}{8}\sqrt{(l+1)l}(l-1)(l-2)R_{l-3}^0 - \frac{1}{8}\sqrt{(l+1)l(l-1)(l-2)(l-3)(l-4)}R_{l-3}^{-2} \quad \text{(E.35)}$$

$$\frac{\partial^3}{\partial x_2^3}(R_l^1) = \frac{i}{8}\sqrt{(l-1)(l-2)(l-3)(l-4)(l-5)(l-6)}R_{l-3}^4 + \frac{3i}{8}\sqrt{(l+1)l(l-1)(l-2)(l-3)(l-4)}R_{l-3}^2 + \frac{3i}{8}\sqrt{(l+1)l}(l-1)(l-2)R_{l-3}^0 + \frac{i}{8}\sqrt{(l+1)l(l-1)(l-2)(l-3)(l-4)}R_{l-3}^{-2} \quad \text{(E.36)}$$

$$\frac{\partial^3}{\partial x_3^3}(R_l^1) = \sqrt{(l+1)l(l-1)^2(l-2)(l-3)}R_{l-3}^1 \quad \text{(E.37)}$$

$$\frac{\partial^3}{\partial x_1^2 \partial x_2}(R_l^1) = -\frac{i}{8}\sqrt{(l-1)(l-2)(l-3)(l-4)(l-5)(l-6)}R_{l-3}^4 + \frac{i}{8}\sqrt{(l+1)l(l-1)(l-2)(l-3)(l-4)}R_{l-3}^2 + \frac{i}{8}\sqrt{(l+1)l}(l-1)(l-2)R_{l-3}^0 - \frac{i}{8}\sqrt{(l+1)l(l-1)(l-2)(l-3)(l-4)}R_{l-3}^{-2} \quad \text{(E.38)}$$

$$\frac{\partial^3}{\partial x_1^2 \partial x_3}(R_l^1) = \frac{1}{4}\sqrt{(l+1)(l-1)(l-2)(l-3)(l-4)(l-5)}R_{l-3}^3 - \frac{1}{2}\sqrt{(l+1)l(l-1)^2(l-2)(l-3)}R_{l-3}^1 - \frac{1}{4}\sqrt{(l+1)l(l-1)^2(l-2)(l-3)}R_{l-3}^{-1} \quad \text{(E.39)}$$

$$\frac{\partial^3}{\partial x_1 \partial x_2^2}(R_l^1) = -\frac{1}{8}\sqrt{(l-1)(l-2)(l-3)(l-4)(l-5)(l-6)}R_{l-3}^4 - \frac{1}{8}\sqrt{(l+1)l(l-1)(l-2)(l-3)(l-4)}R_{l-3}^2 + \frac{1}{8}\sqrt{(l+1)l}(l-1)(l-2)R_{l-3}^0 + \frac{1}{8}\sqrt{(l+1)l(l-1)(l-2)(l-3)(l-4)}R_{l-3}^{-2} \quad \text{(E.40)}$$

$$\frac{\partial^3}{\partial x_2^2 \partial x_3}(R_l^1) = -\frac{1}{4}\sqrt{(l+1)(l-1)(l-2)(l-3)(l-4)(l-5)}R_{l-3}^3 - \frac{1}{2}\sqrt{(l+1)l(l-1)^2(l-2)(l-3)}R_{l-3}^1 + \frac{1}{4}\sqrt{(l+1)l(l-1)^2(l-2)(l-3)}R_{l-3}^{-1} \quad \text{(E.41)}$$

$$\frac{\partial^3}{\partial x_1 \partial x_3^2}(R_l^1) = \frac{1}{2}\sqrt{(l+1)l(l-1)(l-2)(l-3)(l-4)}R_{l-3}^2 - \frac{1}{2}\sqrt{(l+1)l}(l-1)(l-2)R_{l-3}^0 \tag{E.42}$$

$$\frac{\partial^3}{\partial x_2 \partial x_3^2}(R_l^1) = -\frac{i}{2}\sqrt{(l+1)l(l-1)(l-2)(l-3)(l-4)}R_{l-3}^2 - \frac{i}{2}\sqrt{(l+1)l}(l-1)(l-2)R_{l-3}^0 \tag{E.43}$$

$$\frac{\partial^3}{\partial x_1 \partial x_2 \partial x_3}(R_l^1) = -\frac{i}{4}\sqrt{(l+1)(l-1)(l-2)(l-3)(l-4)(l-5)}R_{l-3}^3 - \frac{i}{4}\sqrt{(l+1)l(l-1)^2(l-2)(l-3)}R_{l-3}^{-1} \tag{E.44}$$

- $m = 2$

$$\frac{\partial^3}{\partial x_1^3}(R_l^2) = \frac{1}{8}\sqrt{(l-2)(l-3)(l-4)(l-5)(l-6)(l-7)}R_{l-3}^5 - \frac{3}{8}\sqrt{(l+2)(l+1)(l-2)(l-3)(l-4)(l-5)}R_{l-3}^3 + \frac{3}{8}\sqrt{(l+2)(l+1)l(l-1)(l-2)(l-3)}R_{l-3}^1 + \frac{1}{8}\sqrt{(l+2)(l+1)l(l-1)(l-2)(l-3)}R_{l-3}^{-1} \tag{E.45}$$

$$\frac{\partial^3}{\partial x_2^3}(R_l^2) = \frac{i}{8}\sqrt{(l-2)(l-3)(l-4)(l-5)(l-6)(l-7)}R_{l-3}^5 + \frac{3i}{8}\sqrt{(l+2)(l+1)(l-2)(l-3)(l-4)(l-5)}R_{l-3}^3 + \frac{3i}{8}\sqrt{(l+2)(l+1)l(l-1)(l-2)(l-3)}R_{l-3}^1 - \frac{i}{8}\sqrt{(l+2)(l+1)l(l-1)(l-2)(l-3)}R_{l-3}^{-1} \tag{E.46}$$

$$\frac{\partial^3}{\partial x_3^3}(R_l^2) = \sqrt{(l+2)(l+1)l(l-2)(l-3)(l-4)}R_{l-3}^2 \tag{E.47}$$

$$\frac{\partial^3}{\partial x_1^2 \partial x_2}(R_l^2) = -\frac{i}{8}\sqrt{(l-2)(l-3)(l-4)(l-5)(l-6)(l-7)}R_{l-3}^5 + \frac{i}{8}\sqrt{(l+2)(l+1)(l-2)(l-3)(l-4)(l-5)}R_{l-3}^3 + \frac{i}{8}\sqrt{(l+2)(l+1)l(l-1)(l-2)(l-3)}R_{l-3}^1 + \frac{i}{8}\sqrt{(l+2)(l+1)l(l-1)(l-2)(l-3)}R_{l-3}^{-1} \tag{E.48}$$

$$\frac{\partial^3}{\partial x_1^2 \partial x_3}(R_l^2) = \frac{1}{4}\sqrt{(l+2)(l-2)(l-3)(l-4)(l-5)(l-6)}R_{l-3}^4 - \frac{1}{2}\sqrt{(l+2)(l+1)l(l-2)(l-3)(l-4)}R_{l-3}^2 + \frac{1}{4}\sqrt{(l+2)(l+1)l(l-1)(l-2)^2}R_{l-3}^0 \tag{E.49}$$

$$\frac{\partial^3}{\partial x_1 \partial x_2^2}(R_l^2) = -\frac{1}{8}\sqrt{(l-2)(l-3)(l-4)(l-5)(l-6)(l-7)}R_{l-3}^5 - \frac{1}{8}\sqrt{(l+2)(l+1)(l-2)(l-3)(l-4)(l-5)}R_{l-3}^3 + \frac{1}{8}\sqrt{(l+2)(l+1)l(l-1)(l-2)(l-3)}R_{l-3}^1 - \frac{1}{8}\sqrt{(l+2)(l+1)l(l-1)(l-2)(l-3)}R_{l-3}^{-1} \quad \text{(E.50)}$$

$$\frac{\partial^3}{\partial x_2^2 \partial x_3}(R_l^2) = -\frac{1}{4}\sqrt{(l+2)(l-2)(l-3)(l-4)(l-5)(l-6)}R_{l-3}^4 - \frac{1}{2}\sqrt{(l+2)(l+1)l(l-2)(l-3)(l-4)}R_{l-3}^2 - \frac{1}{4}\sqrt{(l+2)(l+1)l(l-1)(l-2)^2}R_{l-3}^0 \quad \text{(E.51)}$$

$$\frac{\partial^3}{\partial x_1 \partial x_3^2}(R_l^2) = \frac{1}{2}\sqrt{(l+2)(l+1)(l-2)(l-3)(l-4)(l-5)}R_{l-3}^3 - \frac{1}{2}\sqrt{(l+2)(l+1)l(l-1)(l-2)(l-3)}R_{l-3}^1 \quad \text{(E.52)}$$

$$\frac{\partial^3}{\partial x_2 \partial x_3^2}(R_l^2) = -\frac{i}{2}\sqrt{(l+2)(l+1)(l-2)(l-3)(l-4)(l-5)}R_{l-3}^3 - \frac{i}{2}\sqrt{(l+2)(l+1)l(l-1)(l-2)(l-3)}R_{l-3}^1 \quad \text{(E.53)}$$

$$\frac{\partial^3}{\partial x_1 \partial x_2 \partial x_3}(R_l^2) = -\frac{i}{4}\sqrt{(l+2)(l-2)(l-3)(l-4)(l-5)(l-6)}R_{l-3}^4 + \frac{i}{4}\sqrt{(l+2)(l+1)l(l-1)(l-2)^2}R_{l-3}^0 \quad \text{(E.54)}$$

- $m \geq 3$

$$\frac{\partial^3}{\partial x_1^3}(R_l^m) = \frac{1}{8}\sqrt{(l-m)(l-m-1)(l-m-2)(l-m-3)(l-m-4)(l-m-5)}R_{l-3}^{m+3} - \frac{3}{8}\sqrt{(l+m)(l+m-1)(l-m)(l-m-1)(l-m-2)(l-m-3)}R_{l-3}^{m+1} + \frac{3}{8}\sqrt{(l+m)(l+m-1)(l+m-2)(l+m-3)(l-m)(l-m-1)}R_{l-3}^{m-1} - \frac{1}{8}\sqrt{(l+m)(l+m-1)(l+m-2)(l+m-3)(l+m-4)(l+m-5)}R_{l-3}^{m-3} \quad \text{(E.55)}$$

$$\frac{\partial^3}{\partial x_2^3}(R_l^m) = \frac{i}{8}\sqrt{(l-m)(l-m-1)(l-m-2)(l-m-3)(l-m-4)(l-m-5)}R_{l-3}^{m+3} + \frac{3i}{8}\sqrt{(l+m)(l+m-1)(l-m)(l-m-1)(l-m-2)(l-m-3)}R_{l-3}^{m+1} + \frac{3i}{8}\sqrt{(l+m)(l+m-1)(l+m-2)(l+m-3)(l-m)(l-m-1)}R_{l-3}^{m-1} + \frac{i}{8}\sqrt{(l+m)(l+m-1)(l+m-2)(l+m-3)(l+m-4)(l+m-5)}R_{l-3}^{m-3} \tag{E.56}$$

$$\frac{\partial^3}{\partial x_3^3}(R_l^m) = \sqrt{(l+m)(l+m-1)(l+m-2)(l-m)(l-m-1)(l-m-2)}R_{l-3}^{m} \tag{E.57}$$

$$\frac{\partial^3}{\partial x_1^2 \partial x_2}(R_l^m) = -\frac{i}{8}\sqrt{(l-m)(l-m-1)(l-m-2)(l-m-3)(l-m-4)(l-m-5)}R_{l-3}^{m+3} + \frac{i}{8}\sqrt{(l+m)(l+m-1)(l-m)(l-m-1)(l-m-2)(l-m-3)}R_{l-3}^{m+1} + \frac{i}{8}\sqrt{(l+m)(l+m-1)(l+m-2)(l+m-3)(l-m)(l-m-1)}R_{l-3}^{m-1} - \frac{i}{8}\sqrt{(l+m)(l+m-1)(l+m-2)(l+m-3)(l+m-4)(l+m-5)}R_{l-3}^{m-3} \tag{E.58}$$

$$\frac{\partial^3}{\partial x_1^2 \partial x_3}(R_l^m) = \frac{1}{4}\sqrt{(l+m)(l-m)(l-m-1)(l-m-2)(l-m-3)(l-m-4)}R_{l-3}^{m+2} - \frac{1}{2}\sqrt{(l+m)(l+m-1)(l+m-2)(l-m)(l-m-1)(l-m-2)}R_{l-3}^{m} + \frac{1}{4}\sqrt{(l+m)(l+m-1)(l+m-2)(l+m-3)(l+m-4)(l-m)}R_{l-3}^{m-2} \tag{E.59}$$

$$\frac{\partial^3}{\partial x_1 \partial x_2^2}(R_l^m) = -\frac{1}{8}\sqrt{(l-m)(l-m-1)(l-m-2)(l-m-3)(l-m-4)(l-m-5)}R_{l-3}^{m+3} - \frac{1}{8}\sqrt{(l+m)(l+m-1)(l-m)(l-m-1)(l-m-2)(l-m-3)}R_{l-3}^{m+1} + \frac{1}{8}\sqrt{(l+m)(l+m-1)(l+m-2)(l+m-3)(l-m)(l-m-1)}R_{l-3}^{m-1} + \frac{1}{8}\sqrt{(l+m)(l+m-1)(l+m-2)(l+m-3)(l+m-4)(l+m-5)}R_{l-3}^{m-3} \tag{E.60}$$

$$\frac{\partial^3}{\partial x_2^2 \partial x_3}(R_l^m) = -\frac{1}{4}\sqrt{(l+m)(l-m)(l-m-1)(l-m-2)(l-m-3)(l-m-4)}R_{l-3}^{m+2} - \frac{1}{2}\sqrt{(l+m)(l+m-1)(l+m-2)(l-m)(l-m-1)(l-m-2)}R_{l-3}^{m} - \frac{1}{4}\sqrt{(l+m)(l+m-1)(l+m-2)(l+m-3)(l+m-4)(l-m)}R_{l-3}^{m-2} \tag{E.61}$$

$$\frac{\partial^3}{\partial x_1 \partial x_3^2}(R_l^m) = \frac{1}{2}\sqrt{(l+m)(l+m-1)(l-m)(l-m-1)(l-m-2)(l-m-3)}R_{l-3}^{m+1} - \frac{1}{2}\sqrt{(l+m)(l+m-1)(l+m-2)(l+m-3)(l-m)(l-m-1)}R_{l-3}^{m-1} \quad \text{(E.62)}$$

$$\frac{\partial^3}{\partial x_2 \partial x_3^2}(R_l^m) = -\frac{i}{2}\sqrt{(l+m)(l+m-1)(l-m)(l-m-1)(l-m-2)(l-m-3)}R_{l-3}^{m+1} - \frac{i}{2}\sqrt{(l+m)(l+m-1)(l+m-2)(l+m-3)(l-m)(l-m-1)}R_{l-3}^{m-1} \quad \text{(E.63)}$$

$$\frac{\partial^3}{\partial x_1 \partial x_2 \partial x_3}(R_l^m) = -\frac{i}{4}\sqrt{(l+m)(l-m)(l-m-1)(l-m-2)(l-m-3)(l-m-4)}R_{l-3}^{m+2} + \frac{i}{4}\sqrt{(l+m)(l+m-1)(l+m-2)(l+m-3)(l+m-4)(l-m)}R_{l-3}^{m-2} \quad \text{(E.64)}$$

Appendix F. Correction ε^0 to the dipolar field

The field which must be subtracted from the discrete sum of the dipolar field over neighbour boxes, in order to get a periodic solution, has an analytical form if the sum is performed over a cuboid domain centered on the similation box [48]. We recall here its expression for the sake of completeness. Let the dimensions of the summation domain be l_1, l_2 and l_3. We have for the two components ε_{11}^0 and ε_{12}^0 (other terms are obtained by cyclic permutation of indices):

$$\varepsilon_{11}^0 = \frac{p_{11}}{2\pi(1-\nu)\mu}\left[2(1-2\nu)A(l_1,l_2,l_3) + B(l_1,l_2,l_3)\right] - \frac{p_{22}}{2\pi(1-\nu)\mu}E(l_2,l_1,l_3) - \frac{p_{33}}{2\pi(1-\nu)\mu}E(l_3,l_1,l_2) \quad \text{(F.1)}$$

$$\varepsilon_{12}^0 = \frac{p_{12}}{2\pi(1-\nu)\mu}\left[2(1-\nu)\left(A(l_1,l_2,l_3)+A(l_2,l_1,l_3)\right) - \left(E(l_1,l_2,l_3)+E(l_2,l_1,l_3)\right)\right]. \quad \text{(F.2)}$$

Functions A, B and E are given by

$$A(x,y,z) = \arctan\left(\frac{yz}{x\sqrt{x^2+y^2+z^2}}\right) \quad \text{(F.3)}$$

$$B(x,y,z) = \frac{xyz(2x^2+y^2+z^2)}{(x^2+y^2)(x^2+z^2)\sqrt{x^2+y^2+z^2}} \quad \text{(F.4)}$$

$$E(x,y,z) = \frac{xyz}{(x^2+y^2)\sqrt{x^2+y^2+z^2}}. \quad \text{(F.5)}$$

References

[1] S. J. Zinkle. Radiation-induced effects on microstructure. In R. J. M. Konings and R. E. Stoller, editors, *Comprehensive Nuclear Materials*, chapter 1.04, page 91. Elsevier, second edition, 2020.

[2] A. D. Brailsford and R. Bullough. The rate theory of swelling due to void growth in irradiated metals. *J. Nucl. Mater.*, 44:121, 1972.

[3] T. Jourdan and M. Nastar. On the relative contributions of point defect clusters to macroscopic swelling of metals. *J. Appl. Phys.*, 131:225103, 2022.

[4] M. J. Caturla, N. Soneda, E. Alonso, B. D. Wirth, T. Diaz de la Rubia, and J. M. Perlado. Comparative study of radiation damage accumulation in Cu and Fe. *J. Nucl. Mater.*, 276:13, 2000.

[5] C. Domain, C. S. Becquart, and L. Malerba. Simulation of radiation damage in Fe alloys: an object kinetic Monte Carlo approach. *J. Nucl. Mater.*, 335:121, 2004.

[6] J. Dalla Torre, C.-C. Fu, F. Willaime, A. Barbu, and J.-L. Bocquet. Resistivity recovery simulations of electron-irradiated iron: Kinetic Monte Carlo versus cluster dynamics. *J Nucl Mater*, 352:42, 2006.

[7] I. Martin-Bragado, A. Rivera, G. Valles, J. L. Gomez-Selles, and M. J. Caturla. MMonCa: An Object Kinetic Monte Carlo simulator for damage irradiation evolution and defect diffusion. *Comput. Phys. Commun.*, 184(12):2703, 2013.

[8] E. Martinez, M. J. Caturla, and J. Marian. *DFT-Parameterized Object Kinetic Monte Carlo Simulations of Radiation Damage*, page 2457. Springer International Publishing, 2020.

[9] N. M. Ghoniem, S. H. Tong, J. Huang, B. N. Singh, and M. Wen. Mechanisms of dislocation-defect interactions in irradiated metals investigated by computer simulations. *J. Nucl. Mater.*, 307-311:843, 2002.

[10] A. B. Sivak, V. M. Chernov, V. A. Romanov, and P. A. Sivak. Kinetic Monte-Carlo simulation of self-point defect diffusion in dislocation elastic fields in bcc iron and vanadium. *J. Nucl. Mater.*, 417:1067, 2011.

[11] G. Subramanian, D. Perez, B. P. Uberuaga, C. N. Tomé, and A. F. Voter. Method to account for arbitrary strains in kinetic Monte Carlo simulations. *Phys. Rev. B*, 87:144107, 2013.

[12] A. Vattré, T. Jourdan, H. Ding, M.-C. Marinica, and M. J. Demkowicz. Non-random walk diffusion enhances the sink strength of semicoherent interfaces. *Nat. Commun.*, 7:10424, 2016.

[13] D. Carpentier, T. Jourdan, Y. Le Bouar, and M.-C. Marinica. Effect of saddle point anisotropy of point defects on their absorption by dislocations and cavities. *Acta Mater.*, 136:323, 2017.

[14] T. Jourdan and A. Vattré. A continuous model including elastodiffusion for sink strength calculation of interfaces. *Comput. Mater. Sci.*, 153:473, 2018.

[15] D. R. Mason, X. Yi, M. A. Kirk, and S. L. Dudarev. Elastic trapping of dislocation loops in cascades in ion-irradiated tungsten foils. *J. Phys.: Condens. Matter*, 26:375701, 2014.

[16] D. Carpentier, T. Jourdan, P. Terrier, M. Athènes, and Y. Le Bouar. Effect of sink strength dispersion on cluster size distributions simulated by cluster dynamics. *J. Nucl. Mater.*, 533:152068, 2020.

[17] A. A. Kohnert and L. Capolungo. Sink strength and dislocation bias of three-dimensional microstructures. *Phys. Rev. Mater.*, 3:053608, 2019.

[18] H. Moulinec and P. Suquet. A fast numerical method for computing the linear and nonlinear mechanical properties of composites. *C. R. Acad. Sci. Paris, Ser. II*, 318:1417, 1994.

[19] S. Y. Hu and L. Q. Chen. Solute segregation and coherent nucleation and growth near a dislocation – a phase-field model integrating defect and phase microstructures. *Acta Mater.*, 49:463, 2001.

[20] D. Rodney, Y. Le Bouar, and A. Finel. Phase field methods and dislocations. *Acta Mater.*, 51:17, 2003.

[21] N. Bertin, M. V. Upadhyay, C. Pradalier, and L. Capolungo. A FFT-based formulation for efficient mechanical fields computation in isotropic and anisotropic periodic discrete dislocation dynamics. *Modell. Simul. Mater. Sci. Eng.*, 23:065009, 2015.

[22] J. T. Graham, A. D. Rollett, and R. LeSar. Fast Fourier transform discrete dislocation dynamics. *Modell. Simul. Mater. Sci. Eng.*, 24:085005, 2016.

[23] R. LeSar and L. Capolungo. *Advances in Discrete Dislocation Dynamics Simulations*, page 1079. Springer International Publishing, 2020.

[24] L. Greengard and V. Rokhlin. Rapid evaluation of potential fields in three dimensions. In C. Anderson and C. Greengard, editors, *Vortex Methods*, volume 1360 of *Lectures Notes in Mathematics*, page 121. Springer-Verlag, Berlin, 1988.

[25] H. Cheng, L. Greengard, and V. Rokhlin. A fast adaptive multipole algorithm in three dimensions. *J. Comput. Phys.*, 155:468, 1999.

[26] A. Arsenlis, W. Cai, M. Tang, M. Rhee, T. Opplestrup, G. Hommes, T. G. Pierce, and V. V. Bulatov. Enabling strain hardening simulations with dislocation dynamics. *Modelling Simul. Mater. Sci. Eng.*, 15:553, 2007.

[27] D. Zhao, J. Huang, and Y. Xiang. A new version fast multipole method for evaluating the stress field of dislocation ensembles. *Modelling Simul. Mater. Sci. Eng.*, 18:045006, 2010.

[28] C. Chen, S. Aubry, T. Oppelstrup, A. Arsenlis, and E. Darve. Fast algorithms for evaluating the stress field of dislocation lines in anisotropic elastic media. *Modell. Simul. Mater. Sci. Eng.*, 26:045007, 2018.

[29] Daniel T. Gillespie. A general method for numerically simulating the stochastic time evolution of coupled chemical reactions. *J. Comput. Phys.*, 22:403, 1976.

[30] A. B. Bortz, M. H. Kalos, and J. L. Lebowitz. A New Algorithm for Monte-Carlo Simulation of Ising Spin Systems. *J. Comput. Phys.*, 17:10, 1975.

[31] T. Jourdan. Enforcing local equilibrium of point defects near sinks in object kinetic monte carlo simulations. *Modell. Simul. Mater. Sci. Eng.*, 29:035007, 2021.

[32] R. Siems. Mechanical interactions of point defects. *Phys. Stat. Sol.*, 30:645, 1968.

[33] E. Clouet, C. Varvenne, and T. Jourdan. Elastic modeling of point-defects and their interactions. *Comp. Mater. Sci.*, 147:49, 2018.

[34] N. M. Ghoniem and L. Z. Sun. Fast-sum method for the elastic field of three-dimensional dislocation ensembles. *Phys. Rev. B*, 60:128, 1999.

[35] J. P. Hirth and J. Lothe. *Theory of dislocations*. McGraw-Hill, 1968.

[36] T. Mura. *Micromechanics of defects in solids*. Martinus Nijhoff, 1987.

[37] W. G. Wolfer and M. Ashkin. Stress-induced diffusion of point defects to spherical sinks. *J. Appl. Phys.*, 46:547, 1975.

[38] V. A. Borodin, A. I. Ryazanov, and C. Abromeit. Void bias factors due to the anisotropy of the point defect diffusion. *J. Nucl. Mater.*, 207:242, 1993.

[39] N. A. Gumerov and R. Duraiswami. Fast multipole method for the biharmonic equation in three dimensions. *J. Comput. Phys.*, 215:363, 2006.

[40] H. Y. Wang and R. LeSar. An efficient fast-multipole algorithm based on an expansion in the solid harmonics. *J. Chem. Phys.*, 104:4173, 1996.

[41] C. H. Choi, J. Ivanic, M. S. Gordon, and K. Ruedenberg. Rapid and stable determination of rotation matrices between spherical harmonics by direct recursion. *J. Chem. Phys.*, 111:8825, 1999.

[42] G. B. Arfken and H. J. Weber. *Mathematical Methods for Physicists*. Elsevier, 2005.

[43] Y. Fu, K. J. Klimkowski, G. J. Rodin, E. Berger, J. C. Browne, J. K. Singer, R. A. van de Geijn, and K. S. Vemaganti. A fast solution method for three-dimensional many-particle problems of linear elasticity. *Int. J. Numer. Meth. Eng.*, 42:1215, 1998.

[44] Y. Fu and G. J. Rodin. Fast solution method for three-dimensional Stokes many-particle problems. *Commun. Numer. Meth. Eng.*, 16:145, 2000.

[45] T. Jourdan, F. Lançon, and A. Marty. Pinning of magnetic domain walls to structural defects in thin layers within a Heisenberg-type model. *Phys. Rev. B*, 75:094422, 2007.

[46] C. G. Lambert, T. A. Darden, and J. A. Board Jr. A multipole-based algorithm for efficient calculation of forces and potentials in macroscopic periodic assemblies of particles. *J. Comput.*

Phys., 126:274, 1996.

[47] W. Cai, V. V. Bulatov, J. Chang, J. Li, and S. Yip. Periodic image effects in dislocation modelling. *Philos. Mag.*, 83(5):539, 2003.

[48] T. Jourdan. Simulation of macroscopic systems with non-vanishing elastic dipole components. *J. Mech. Phys. Solids*, 125:762, 2019.

[49] G. Leibfried and N. Breuer. Point Defects in Metals I. In *Springer Tracts in Modern Physics*. Springer-Verlag, Berlin, 1978.

[50] E. van der Giessen and A. Needleman. Discrete dislocation plasticity: a simple planar model. *Modelling Simul. Mater. Sci. Eng.*, 3:689, 1995.

[51] D. Braess. *Finite elements : Theory, fast solvers, and applications in solid mechanics*. Cambridge University Press, 1997.

[52] F. Baraglia and P.-W. Ma. Dynamic model for an ensemble of interacting irradiation-induced defects in a macroscopic sample. *Modell. Simul. Mater. Sci. Eng.*, 29:025004, 2021.

[53] M. Kuchta, K.-A. Mardal, and M. Mortensen. On the singular Neumann problem in linear elasticity. *Numer. Linear Algebra Appl.*, 26(1):e2212, 2019.

[54] M. S. Alnæs, J. Blechta, J. Hake, A. Johansson, B. Kehlet, A. Logg, C. Richardson, J. Ring, M. E. Rognes, and G. N. Wells. The FEniCS Project Version 1.5. *Archive of Numerical Software*, 3(100):9, 2015.

[55] C. Geuzaine and J.-F. Remacle. Gmsh: a three-dimensional finite element mesh generator with built-in pre- and post-processing facilities. *Int. J. Numer. Methods Eng.*, 79(11):1309, 2009.

[56] H. L. Heinisch, B. N. Singh, and S. I. Golubov. The effects of one-dimensional glide on the reaction kinetics of interstitial clusters. *J. Nucl. Mater.*, 283–287:737, 2000.

[57] A. Seeger and U. Gösele. Steady-state diffusion of point defects to dislocation loops. *Phys. Lett. A*, 61:423, 1977.

[58] B. Vigeholm and M. J. Makin. The effect of solute concentration on the formation of loops in aluminium-magnesium alloys during fission fragment irradiation. *Phys. Stat. Sol.*, 12:877, 1965.

[59] D. I. R. Norris. The use of the high voltage electron microscope to simulate fast neutron-induced void swelling in metals. *J. Nucl. Mater.*, 40:66, 1971.

[60] K. Ma, B. Décamps, A. Fraczkiewicz, T. Jourdan, F. Prima, and M. Loyer-Prost. Free surface impact on radiation damage in pure nickel by in-situ self-irradiation: can it be avoided? *Acta Mater.*, 212:116874, 2021.

[61] A. Barbu, C. S. Becquart, J.-L. Bocquet, J. Dalla Torre, and C. Domain. Comparison between three complementary approaches to simulate 'large' fluence irradiation: application to electron irradiation of thin foils. *Philos. Mag.*, 85:541, 2005.

[62] K. Urban. Growth of defect clusters in thin nickel foils during electron irradiation. *Phys. Stat. Sol. (a)*, 4:761, 1971.

[63] M. Kiritani, N. Yoshida, H. Takata, and Y. Maehara. Growth of interstitial type dislocation loops and vacancy mobility in electron irradiated materials. *J. Phys. Soc. Jpn*, 38(6):1677, 1975.

[64] S. Jitsukawa and K. Hojou. Effect of temperature and flux change on the behavior of radiation induced dislocation loops in pure aluminum. *J. Nucl. Mater.*, 212-215:221–225, 1994.

[65] R. Bullough, D. W. Wells, J. R. Willis, and M. H. Wood. The interaction energy between interstitial atoms and dislocations and its relevance to irradiation damage processes. In M. F. Ashby, R. Bullough, C. S. Hartley, and J. P. Hirth, editors, *Dislocation Modelling of Physical Systems*, page 116. Pergamon, 1981.

[66] H. Rouchette, L. Thuinet, A. Legris, A. Ambard, and C. Domain. Numerical evaluation of dislocation loop sink strengths: A phase-field approach. *Nucl. Instr. Meth. B*, 352:31, 2015.

[67] D. Carpentier. *Simulation of the absorption kinetics of point defects by dislocations and defect clusters*. PhD thesis, Université Paris-Saclay, 2018.

[68] R. J. A. Tough and A. J. Stone. Properties of the regular and irregular solid harmonics. *J. Phys. A: Math. Gen.*, 10:1261, 1977.